DIPLOMARBEIT

ANTENNA CHARACTERIZATION IN THE NEAR-FIELD

ausgeführt im Rahmen des Christian Doppler Labors
zum Zwecke der Erlangung des akademischen Grades
eines Diplom-Ingenieurs

von

DAVID LÖSCHENBRAND

Matrikelnummer: 0926714
Wattgasse 72/17
1170 Wien

am

Institute of Telecommunications
Fakultät für Elektrotechnik und Informationstechnik
Technische Universität Wien

unter der Leitung von
Univ.Prof. Dipl.-Ing. Dr.-Ing. Christoph Mecklenbräuker
Dipl.-Ing. Dr. techn. Robert Langwieser

Wien, Juni 2016

TECHNISCHE
UNIVERSITÄT
WIEN

institute of
telecommunications

ABSTRACT

Characterization of large antenna structures at high frequencies requires a considerable amount of measurement time. This thesis establishes methods to decrease measurement time while maintaining accuracy by introducing and exploiting sparsity in the multipole coefficient domain. By means of compressed sensing principles the number of samples required in antenna characterization is reduced by 75% as compared to standard techniques. If implemented appropriately this allows for significantly reduced measurement times.

In the beginning, the spherical multipole expansion in combination with optimized translation and rotation operations is introduced and identified as a sparsity transform. In this context, a novel kind of antenna phase center estimation based on a 1-norm minimization is demonstrated. The subsequent discussion of compressed sensing in antenna theory in general and the uniform uncertainty principle in particular provide empirical bounds on the number of samples necessary to reconstruct radiated fields and the corresponding multipole coefficients. These bounds are derived using the worst case scenario of a maximum directivity antenna. Moreover, truncation handling by applying compressed sensing techniques is outlined. An evaluation of the proposed methods concludes the thesis. Solver parameters for the numerical minimization are identified and an iterative algorithm for non-sparse antennas is introduced which accomplishes the reconstruction in an optimized coordinate system, thus enabling its application for a large variety of antennas. The reconstruction of both synthetic and real world antenna data using only 25% of the usually required sampling points demonstrates the functionality of the new methods and their compliance with the empirical bounds.

ZUSAMMENFASSUNG

Der Trend zu hohen Sendefrequenzen im Telekommunikationsbereich resultiert in sehr langen Messzeiten, die für die Charakterisierung großer Antennen notwendig sind. Diese Arbeit führt eine Vorgehensweise ein, die die Anzahl an notwendigen Messpunkten um 75% verringert, ohne die Genauigkeit wesentlich zu beeinflussen. Dazu werden Ergebnisse aus dem Umfeld des sogenannten Compressed Sensing verwendet, um die Anzahl an Multipol-Entwicklungskoeffizienten, die für die Beschreibung einer Antenne notwendig sind, zu minimieren und diese Tatsache für die Antennencharakterisierung zu nutzen. Die korrekte Umsetzung dieser Methode führt zu einer signifikanten Verkürzung der Messzeit.

Zu Beginn wird die sphärische Multipol-Entwicklung als mathematische Grundlage eingeführt. Durch die Anwendung von optimierten Translations- und Rotationsoperatoren wird sichergestellt, dass die Anzahl der Koeffizienten in der Multipol-Entwicklung minimal ist und daher Methoden des Compressed Sensing angewandt werden können. In diesem Zusammenhang wird eine neue Abschätzung des Phasenzentrums einer Antenne vorgestellt, die auf einer 1-Norm Minimierung beruht. Die anschließende Auseinandersetzung mit Compressed Sensing im Antennenumfeld, vor allem mit dem Begriff des Uniform-Uncertainty Prinzips, führt zu empirischen Schranken für die Anzahl an Messpunkten, die für die Rekonstruktion der Entwicklungskoeffizienten notwendig sind. Dazu wird als worst case Szenario die Vermessung einer Antenne mit maximaler Direktivität betrachtet. Darüber hinaus wird eine Technik zum Umgang mit eingeschränkten Messbereichen vorgestellt, welche die zuvor entwickelten Methoden anwendet. Den Abschluss bildet eine Evaluierung, in der zunächst die notwendigen numerischen Parameter der Minimierung ermittelt werden. Weiters wird ein iterativer Algorithmus vorgestellt, der die Rekonstruktion der Entwicklungskoeffizienten in einem optimierten Koordinatensystem durchführt und daher auf eine breite Klasse von Antennen angewandt werden kann. Die abschließende Rekonstruktion von synthetischen und gemessenen Antennendaten mit nur 25% der üblicherweise notwendigen Messpunkte demonstriert die Effektivität der vorgestellten Algorithmen.

ACKNOWLEDGEMENTS

CONTENTS

LIST OF TABLES

ACRONYMS

AUT   Antenna Under Test

FFT   Fast Fourier Transform

LS   Least Squares

MRE   Maximum Radial Extent

MRI   Magnetic Resonance Imaging

MSE   Mean Square Error

SQP   Sequential Quadratic Programming

TE   Transversal-Electric

UUP   Uniform Uncertainty Principle

1

INTRODUCTION

In an entirely connected and data-oriented world, antennas play a crucial but mostly invisible role in every kind of information transmission system. The endeavor to increase data rates while minimizing physical size pushes development towards higher and higher transmission frequencies. This trend entails rising measurement time required for precise antenna characterization. At frequencies of up to 40GHz, a spherical scan of a large antenna takes days rather than hours. This thesis employs compressed sensing methods to improve on this restriction and to allow for a faster prototyping process. Measurement time savings of up to 75% are found to be realistic and achievable, all while the accuracy usually found in spherical scanners is maintained.

1.1 OUTLOOK

The first part of this thesis deals with the basics of the spherical multipole expansion and leads to an algorithm for transforming the field of a source to the multipole coefficient domain and vice verca. The coordinate system underlying this transform is the spherical coordinate system depicted in Figure 1.

With this knowledge, new methods are developed for further processing and analysis of antenna measurement data. Translation and rotation of an antenna and their effects on the multipole coefficients are investigated in detail. Chapter 3 and Chapter 4 introduce concepts of compressed sensing and their applicability to antenna theory. First, the notion of phase center and rotational symmetry is established. In a second step, compressed sensing principles are introduced and they are applied to antenna theory. This results in a 1-norm regularization providing significant reduction of measurement points by using sparsity in the spherical multipole coefficient domain. Finally, an iterative scheme is suggested and verified to further reduce measurement time in antenna characterization setups. Figure 2 illustrates the procedure. Instead of utilizing the complete equiangular sampling grid, only a small random subset thereof is sampled and used for characterizing a source, all while maintaining accuracy.

The theoretic discussion of the matter is concluded by a numerical evaluation of the results. Measurements of different antennas and synthetic data are analyzed and the newly developed methods are applied and evaluated. Good agreement of theoretical considerations and numerical evaluation support the validity of the new approaches.
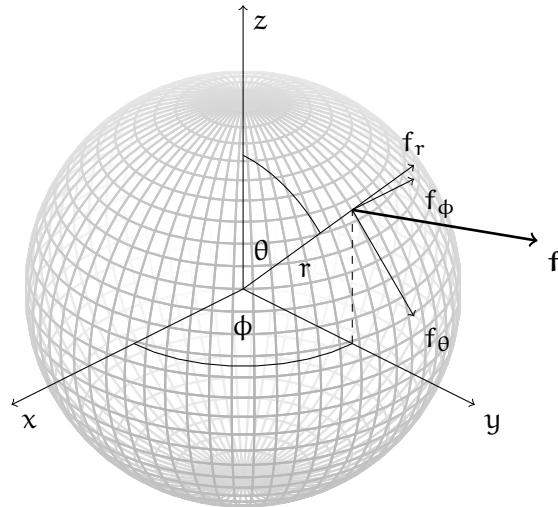
Figure 1: The spherical coordinate system with polar angle θ, azimuth angle ϕ and radial coordinate r. An arbitrary vector $\mathbf{f}$ can be factored into its three components $\mathbf{f}_r$, $\mathbf{f}_\theta$ and $\mathbf{f}_\phi$ with the absolute value of the component $f_r = \mathbf{f} \cdot \hat{\mathbf{r}}$, $f_\theta = \mathbf{f} \cdot \hat{\boldsymbol{\theta}}$ and $f_\phi = \mathbf{f} \cdot \hat{\boldsymbol{\phi}}$, respectively. The notations $\hat{\mathbf{r}}$, $\hat{\boldsymbol{\theta}}$ and $\hat{\boldsymbol{\phi}}$ indicate the unit vector of the respective quantity.

(a) Complete equiangular sampling grid on the sphere.

(b) Random subset of the complete equiangular sampling grid.
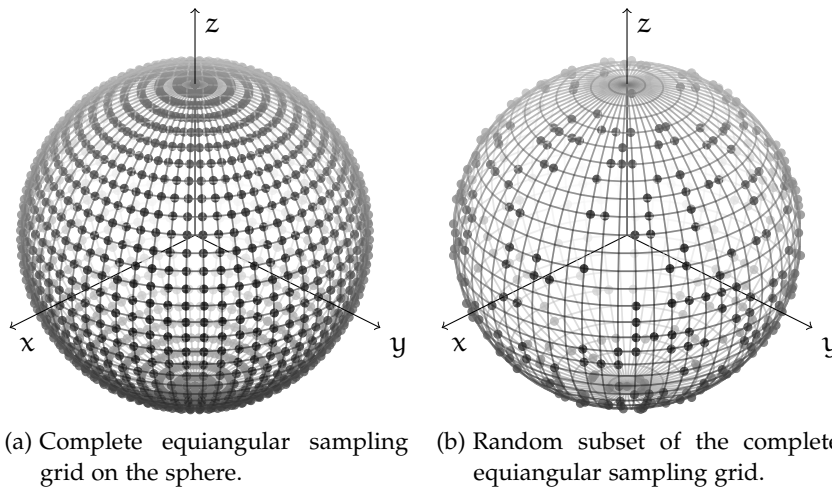
Figure 2: Comparison of the complete equiangular sampling grid and the reduced sampling grid which contains 25% of the sampling points (gray dots).

1.2 LITERATURE OVERVIEW

The near-field to far-field transform has long been a standard tool for antenna characterization in a closed and controllable environment. Of all the different kinds of measurements, the spherical setup provides the most complete and accurate representation for any given antenna since the truncated scan area is smallest. It is, on the other hand, more computationally expensive than its planar and cylindrical counterparts. In [1], a very broad and detailed insight into spherical antenna measurements is provided. The suggested methods for the near-field to far-field transform, probe compensation and measurement setups became quasi-standard in industry and research. More advanced probe compensation methods for high-order probes, which allow a large variety of antennas to be used as probes, can be found in [2, 3]. A near-field to far-field transform using a plane wave expansion and featuring full probe correction is provided in [4]. However, none of the afore mentioned publications includes the case of highly undersampled spherical measurement data.

Accurate determination of the phase center of an antenna is of great interest in global positioning systems, spatial filtering of antenna measurements and broadcasting. Common approaches to this task include Least Squares (LS) solutions [5, 6, 7] and angular momentum minimization [8]. Both methods have the disadvantage of not minimizing the size of the coefficient's supporting set and are therefore not adequate for sampling point reduction via compressed sensing.

One of the earliest and most recognized publications which establishes the term *compressed sensing* is given by [9] where it is proved that partial knowledge of frequency samples allows perfect reconstruction of a sparse signal under certain circumstances. In [10] this methodology is extended to non-exact signals and the term of the *Uniform Uncertainty Principle* is refined. For signals with power law decay, [11] provides error bounds and reconstruction probabilities as well as different measurement ensembles. From the early days, one of the most prominent applications of compressed sensing was the measurement time reduction for medical Magnetic Resonance Imaging (MRI) scans [12]. The close fundamental similarity of MRI scans and antenna scans as well as the use of compressed sensing principles for antenna measurements has, to the best knowledge of the author, never been investigated in detail.

As a short note on the side, it is stated that the personal pronoun *we* will be used throughout the thesis when procedures, approaches and derivations are explained. On the one hand, this prevents the excessive and complicated use of passive voice when it is not suitable. On the other hand, it invites the reader to follow the author's stream of thoughts and decisions through the thesis.

SPHERICAL MULTIPOLE EXPANSION

The spherical multipole expansion is broadly used in the field of electrical engineering. Wave propagation, electrostatics and quantum-mechanics are just a few important areas of application. Geophysics and computer graphics employ multipole expansions in spherical coordinates as well. In this chapter, the mathematical fundamentals are presented and their use concerning multipole radiation is investigated. A detailed derivation can be found in [13, Chapter 9], the most important results for this thesis are repeated in what follows.

2.1 SOLVING THE SPHERICAL WAVE EQUATION

Assuming a time dependence of $e^{-i\omega t}$, a source-free region and a lossless, linear, isotropic and homogeneous medium, Maxwell's equations read as

$$
\begin{aligned}
\boldsymbol{\nabla} \times \mathbf{E} &= i\omega\mu\mathbf{H} \\
\boldsymbol{\nabla} \cdot \mathbf{E} &= 0 \\
\boldsymbol{\nabla} \times \mathbf{H} &= -i\omega\epsilon\mathbf{E} \\
\boldsymbol{\nabla} \cdot \mathbf{H} &= 0
\end{aligned}
\tag{1}
$$

with

$\mathbf{E}$	-	electric field
$\mathbf{H}$	-	magnetic field
ω	-	angular frequency
ϵ	-	permittivity of medium
μ	-	permeability of medium.

By applying the curl operator and eliminating $\mathbf{H}$ in Equation 1, we get an equivalent system of equations

$$
\begin{aligned}
\left(\boldsymbol{\nabla}^2 + k^2\right) \mathbf{E} &= 0 \\
\boldsymbol{\nabla} \cdot \mathbf{E} &= 0 \\
\mathbf{H} &= -\frac{i}{\omega\mu}\boldsymbol{\nabla} \times \mathbf{E},
\end{aligned}
\tag{2}
$$

where $k = \omega\sqrt{\epsilon\mu}$ is the propagation constant. Correspondingly, when we eliminate $\mathbf{E}$, we get

$$
\begin{aligned}
\left(\boldsymbol{\nabla}^2 + k^2\right) \mathbf{H} &= 0 \\
\boldsymbol{\nabla} \cdot \mathbf{H} &= 0 \\
\mathbf{E} &= \frac{i}{\omega\epsilon}\boldsymbol{\nabla} \times \mathbf{H}.
\end{aligned}
\tag{3}
$$

With the vector formula

$$\nabla^2(\mathbf{r} \cdot \mathbf{A}) = \mathbf{r} \cdot (\nabla^2 \mathbf{A}) + 2\nabla \cdot \mathbf{A} \tag{4}$$

for a well-behaved vector field $\mathbf{A}$, Equation 1 and Equation 3 we can easily verify that

$$\left(\nabla^2 + k^2\right)(\mathbf{r} \cdot \mathbf{H}) = 2\nabla \cdot \mathbf{H} + \mathbf{r} \cdot \left(\nabla^2 + k^2\right)\mathbf{H} = 0 \tag{5}$$

holds for the scalar $\mathbf{r} \cdot \mathbf{H}$. This quantity is introduced as an intermediate step because it facilitates the derivation of a spherical mode expansion of the electromagnetic field. A general solution

$$\mathbf{r} \cdot \mathbf{H} = \sum_{n=0}^{\infty} \sum_{m=-n}^{n} \left[A_{nm}^{(1)} h_n^{(1)}(kr) + A_{nm}^{(2)} h_n^{(2)}(kr)\right] Y_{nm}(\theta, \phi) \tag{6}$$

can be constructed via separation of variables with the quantities

$Y_{nm}(\theta, \phi)$ - spherical harmonics of degree n and order m
$h_n^{(1)}(kr)$ - spherical Hankel function of first kind
$h_n^{(2)}(kr)$ - spherical Hankel function of second kind
$A_{nm}^{(1)}$ - first expansion coefficient
$A_{nm}^{(2)}$ - second expansion coefficient.

The spherical harmonics constitute a complete orthonormal set on the surface of the unit sphere and are defined as

$$Y_{nm}(\theta, \phi) = \sqrt{\frac{2n+1}{4\pi} \frac{(n-m)!}{(n+m)!}} P_n^m(\cos\theta) e^{im\phi} \tag{7}$$

with the Legendre polynomial and associated Legendre function, respectively, given by

$$P_n(\cos\theta) = \frac{1}{2^n n!} \left(\frac{d}{d\cos\theta}\right)^n \left(\cos^2\theta - 1\right)^n \tag{8}$$

$$P_n^m(\cos\theta) = (\sin\theta)^m \left(\frac{d}{d\cos\theta}\right)^m P_n(\cos\theta). \tag{9}$$

The spherical Hankel functions of first and second kind are written as

$$h_n^{(1,2)}(x) = j_n(x) \pm iy_n(x) \tag{10}$$

with the spherical Bessel functions

$$j_n(x) = (-x)^n \left(\frac{1}{x}\frac{d}{dx}\right)^n \frac{\sin x}{x}$$

$$y_n(x) = -(-x)^n \left(\frac{1}{x}\frac{d}{dx}\right)^n \frac{\cos x}{x}. \tag{11}$$

Table 1: Depiction of the spherical harmonics of degree n and order m used for describing the radial component of the electromagnetic field of an arbitrary radiating source.

$Y_{n,m}(\theta, \phi)$	$m=0$	$m=1$	$m=2$	$m=3$	...
$n=1$			$-$	$-$	...
$n=2$				$-$	...
$n=3$					...
$\vdots$	$\vdots$	$\vdots$	$\vdots$	$\vdots$	$\ddots$

For the purpose of this thesis, it is sufficient to consider only out-wards travelling waves with respect to the origin. Further, we will drop the superscript of the coefficient $A_{nm}^{(1)}$. Therefore, Equation 6 reduces to

$$\mathbf{r} \cdot \mathbf{H} = \sum_{n=0}^{\infty} \sum_{m=-n}^{n} A_{nm} h_n^{(1)}(kr) Y_{nm}(\theta, \phi). \tag{12}$$

The *magnetic* summation term of degree n and order m from the expansion in Equation 12 is defined to fulfill the conditions

$$\mathbf{r} \cdot \mathbf{H}_{nm}^{(M)} = \frac{n(n+1)}{k} A_{nm} h_n^{(1)}(kr) Y_{nm}(\theta, \phi)$$
$$\mathbf{r} \cdot \mathbf{E}_{nm}^{(M)} = 0 \tag{13}$$

and is therefore a Transversal-Electric (TE) component of the electromagnetic field. From Equation 2 we have

$$\omega \mu \mathbf{r} \cdot \mathbf{H} = \frac{1}{i} \mathbf{r} \cdot (\boldsymbol{\nabla} \times \mathbf{E}) = \frac{1}{i} (\mathbf{r} \times \boldsymbol{\nabla}) \cdot \mathbf{E} = \mathbf{L} \cdot \mathbf{E} \tag{14}$$

with the operator

$$\mathbf{L} = \frac{1}{i} (\mathbf{r} \times \boldsymbol{\nabla}). \tag{15}$$

Combining Equation 13 and Equation 14 yields

$$\mathbf{L} \cdot \mathbf{E}_{nm}^{(M)} = n(n+1) Z A_{nm} h_n^{(1)}(kr) Y_{nm}(\theta, \phi)$$
$$\mathbf{r} \cdot \mathbf{E}_{nm}^{(M)} = 0 \tag{16}$$

for the electric field. $Z = \sqrt{\mu/\epsilon}$ denotes the wave impedance of the medium. Since

$$L^2 Y_{nm}(\theta, \phi) = n(n+1) Y_{nm}(\theta, \phi), \tag{17}$$

the electromagnetic field of the magnetic term of degree n and order m satisfying the conditions in Equation 16 can be written as

$$\mathbf{E}_{nm}^{(M)} = ZA_{nm}h_n^{(1)}(kr)\mathbf{L}Y_{nm}(\theta, \phi)$$
$$\mathbf{H}_{nm}^{(M)} = -\frac{i}{\omega\mu}\nabla \times \mathbf{E}_{nm}^{(M)}.$$
(18)

A very similar approach leads to the electromagnetic field of the electric mode of degree n and order m

$$\mathbf{H}_{nm}^{(E)} = B_{nm}h_n^{(1)}(kr)\mathbf{L}Y_{nm}(\theta, \phi)$$
$$\mathbf{E}_{nm}^{(E)} = \frac{i}{\omega\epsilon}\nabla \times \mathbf{H}_{nm}^{(E)}.$$
(19)

If we now introduce the normalized vector spherical harmonics

$$\mathbf{X}_{nm} = \frac{1}{\sqrt{n(n+1)}}\mathbf{L}Y_{nm}(\theta, \phi),$$
(20)

the electromagnetic field in a source-free region can be written as

$$\mathbf{H} = \sum_{n,m}\left[a_E(n, m)h_n^{(1)}(kr)\mathbf{X}_{nm}\right.$$
$$\left. -\frac{i}{k}a_M(n, m)\nabla \times h_n^{(1)}(kr)\mathbf{X}_{nm}\right]$$
(21)
$$\mathbf{E} = Z\sum_{n,m}\left[\frac{i}{k}a_E(n, m)\nabla \times h_n^{(1)}(kr)\mathbf{X}_{nm}\right.$$
$$\left. + a_M(n, m)h_n^{(1)}(kr)\mathbf{X}_{nm}\right].$$
(22)

The normalized vector spherical harmonics satisfy the orthogonality relations

$$\int \bar{\mathbf{X}}_{n'm'} \cdot \mathbf{X}_{nm}\, d\Omega = \delta_{nn'}\delta_{mm'}$$
(23)

$$\int \bar{\mathbf{X}}_{n'm'} \cdot (\mathbf{r} \times \mathbf{X}_{nm})\, d\Omega = 0$$
(24)

with

$$\int f(\theta, \phi)\, d\Omega = \int_0^{2\pi}\int_0^{\pi} f(\theta, \phi)\sin\theta\, d\theta\, d\phi$$
(25)

being the integral over the unit sphere and $\bar{z}$ denoting the complex conjugate of z. The spherical wave coefficients used in the above expansion can be calculated according to

$$a_M(n, m)h_n^{(1)}(kr) = \frac{k}{\sqrt{n(n+1)}}\int \bar{Y}_{nm}(\theta, \phi)\mathbf{r} \cdot \mathbf{H}\, d\Omega$$
(26)

$$Za_E(n, m)h_n^{(1)}(kr) = -\frac{k}{\sqrt{n(n+1)}}\int \bar{Y}_{nm}(\theta, \phi)\mathbf{r} \cdot \mathbf{E}\, d\Omega.$$
(27)

This concludes the summary of [13] and is the main result of this Section. It shows that we can calculate the spherical wave coefficients if we know the electric or magnetic field normal to a sphere via an integration over the sphere (cf. Equation 26, Equation 27). Once we determine these coefficients, we can calculate the electric and magnetic field in a source-free region via Equation 21 and Equation 22.

If only the tangential components of the electric field are known, the spherical wave coefficients are obtained by

$$Za_M(n,m)h_n^{(1)}(kr) = \frac{1}{\sqrt{n(n+1)}} \int \bar{Y}_{nm}(\theta,\phi)\mathbf{L}\cdot\mathbf{E}\,d\Omega \qquad (28)$$

$$Zia_E(n,m)\left(krh_{n+1}^{(1)}(kr) - (n+1)h_n^{(1)}(kr)\right)$$
$$= \frac{k}{\sqrt{n(n+1)}} \int (\mathbf{r}\times\mathbf{E})\cdot\mathbf{L}\bar{Y}_{nm}(\theta,\phi)\,d\Omega \qquad (29)$$

what can be verified by substitution into Equation 22.

2.2 A NEAR-FIELD TO FAR-FIELD TRANSFORM

Before we start to develop a near-field to far-field transform, a new notation is introduced for Equation 21 and Equation 22 similar to the one used in [1]. We do this because this notation proves to be more convenient. It is also the most used notation for the multipole expansion in the field of antenna measurements.

2.2.1 Multipole Expansion and Multipole Coefficients

Equation 21 and Equation 22 can be rewritten as

$$\mathbf{H} = \frac{-ik}{\sqrt{Z}} \sum_{smn} Q_{smn}\mathbf{F}_{3-s,m,n} \qquad (30)$$

$$\mathbf{E} = k\sqrt{Z} \sum_{smn} Q_{smn}\mathbf{F}_{smn} \qquad (31)$$

with

$$\sum_{smn} = \sum_{s=1}^{2}\sum_{n=0}^{\infty}\sum_{m=-n}^{n} \cdot \qquad (32)$$

The new spherical multipole coefficients Q_{smn} can be calculated by using

$$Q_{1mn} = \frac{i\sqrt{Z}}{k}\left(\frac{-m}{|m|}\right)^m a_M(n,m)$$
$$Q_{2mn} = \frac{-\sqrt{Z}}{k}\left(\frac{-m}{|m|}\right)^m a_E(n,m), \qquad (33)$$

while the new base functions are defined as

$$F_{mn}(r,\theta,\phi) = \left(\frac{-m}{|m|}\right)^m \frac{1}{\sqrt{n(n+1)}} h_n^{(1)}(kr) Y_{nm}(\theta,\phi)$$
$$\mathbf{F}_{1mn} = \nabla F_{mn}(r,\theta,\phi) \times \mathbf{r} \tag{34}$$
$$\mathbf{F}_{2mn} = k^{-1} \nabla \times \mathbf{F}_{1mn}(r,\theta,\phi).$$

With this notation, the radiated power P of the outwards travelling waves can be easily calculated as (cf. [1])

$$P = \frac{1}{2} \sum_{smn} |Q_{smn}|^2. \tag{35}$$

The power radiated by modes with specific degree n is given by the n-mode power spectrum (cf. [14])

$$P_n = \frac{1}{2} \sum_{s=1}^{2} \sum_{m=-n}^{n} |Q_{smn}|^2. \tag{36}$$

For sources with finite spatial dimension, modes above a certain degree N do not significantly contribute to the expansion in Equation 31 and Equation 30, i.e.

$$P_n = \frac{1}{2} \sum_{s=1}^{2} \sum_{m=-n}^{n} |Q_{smn}|^2 \approx 0 \quad \text{for} \quad n > N. \tag{37}$$

This threshold N is directly linked to how electrically large the source is. A very common value often used in antenna measurements (cf. [1, 14]) is

$$N = \lceil kr_0 \rceil + 10 \tag{38}$$

with r_0 denoting the Maximum Radial Extent (MRE) of the source, i. e. the radius of the sphere centered at the origin and completely enclosing the source. Other values for the cutoff degree N directly related to the required accuracy can be found in [14].

With Equation 37, the multipole expansion of the electromagnetic field can now be approximated as

$$\mathbf{E} \approx k\sqrt{Z} \sum_{smn} Q_{smn} \mathbf{F}_{smn} \tag{39}$$

$$\mathbf{H} \approx \frac{-ik}{\sqrt{Z}} \sum_{smn} Q_{smn} \mathbf{F}_{3-s,m,n} \tag{40}$$

with

$$\sum_{smn} = \sum_{s=1}^{2} \sum_{n=0}^{N} \sum_{m=-n}^{n} \tag{41}$$

and N chosen according to Equation 38.

2.2.2 *The Transmission Formula*

For antenna measurements, the projection of the field onto our orthogonal basis described by Equation 26 and Equation 27 needs some adaptation because we usually do not measure the electric field in one point, we rather obtain a weighted spatial average of the field which depends on the probe antenna. In [1, Chapter 3]. a method to obtain the multipole coefficients Q_{smn} with knowledge of the probe antenna and the field tangential to a sphere enclosing the Antenna Under Test (AUT) is developed. In what follows, his method is summarized and explained for our purpose. For detailed derivations, the reader is referred to the original literature.

The transmission formula

$$w(A, \chi, \theta, \phi) = \frac{1}{2} \sum_{\substack{smn \\ \sigma\mu\nu}} Q_{smn} e^{im\phi} d_{\mu m}^{n}(\theta) e^{i\mu\chi} C_{\sigma\mu\nu}^{sn}(kA) R_{\sigma\mu\nu}^{p} \quad (42)$$

relates the multipole coefficients of the AUT with the output of a perfectly matched probe. The quantities used in the formula are:

$w(A, \chi, \theta, \phi)$	-	probe output at measurement radius A and probe orientation χ
Q_{smn}	-	multipole coefficient of AUT
$d_{\mu m}^{n}(\theta)$	-	rotation coefficient
$C_{\sigma\mu\nu}^{sn}(kA)$	-	translation coefficient
$R_{\sigma\mu\nu}^{p}$	-	probe receiving coefficients.

The definitions for the rotation and translation coefficients are rather lengthy and are therefore omitted here. They can be found in the appendix of [1]. What is important to note is that in combination with the factors $e^{im\phi}$ and $e^{i\mu\chi}$, they account for a coordinate transform of the basis functions from the original coordinate system to the one where the probe receiving coefficients are defined. A simplified notation is used to describe the summation in Equation 42, defined as

$$\sum_{\substack{smn \\ \sigma\mu\nu}} = \sum_{s=1}^{2} \sum_{n=0}^{N} \sum_{m=-n}^{n} \sum_{\mu=-n}^{n} \sum_{\sigma=1}^{2} \sum_{\substack{\nu=|\mu| \\ \nu\neq 0}}^{\infty} . \quad (43)$$

Another simplification in notation arises when all terms depending on the probe and its position are collected into the probe response constants

$$P_{s\mu n}(kA) = \frac{1}{2} \sum_{\sigma\nu} C_{\sigma\mu\nu}^{sn}(kA) R_{\sigma\mu\nu}^{p}, \quad (44)$$

what allows to write Equation 42 as

$$w(A, \chi, \theta, \phi) = \sum_{\substack{smn \\ \mu}} Q_{smn} e^{im\phi} d_{\mu m}^n(\theta) e^{i\mu\chi} P_{s\mu n}(kA).\qquad(45)$$

Solving this equation for the unknown spherical coefficients is usually challenging due to ill conditioning. A distinctive simplification arises when first-order probes are used for measurement purposes, i.e.

$$P_{s\mu n}(kA) \approx 0 \quad \text{for} \quad \mu \neq \pm 1.\qquad(46)$$

Concluding the summary of [1], the coefficients Q_{smn} can be calculated by solving the system of equations

$$\begin{aligned} Q_{1mn}P_{11n}(kA) + Q_{2mn}P_{21n}(kA) &= w_{1m}^n(A) \\ Q_{1mn}P_{1,-1,n}(kA) + Q_{2mn}P_{2,-1,n}(kA) &= w_{-1,m}^n(A) \end{aligned}\qquad(47)$$

with a series of transformations of the input data

$$w_\mu(A, \theta, \phi) = \frac{1}{2\pi} \int_{\chi=0}^{2\pi} w(A, \chi, \theta, \phi) e^{-i\mu\chi} \, d\chi\qquad(48)$$

$$w_{\mu m}(A, \theta) = \frac{1}{2\pi} \int_{\phi=0}^{2\pi} w_\mu(A, \theta, \phi) e^{-im\phi} \, d\phi\qquad(49)$$

$$w_{\mu m}^n(A) = \frac{2n+1}{2} \int_{\theta=0}^{\pi} w_{\mu m}(A, \theta) d_{\mu m}^n(\theta) \sin\theta \, d\theta.\qquad(50)$$

Again, once the spherical coefficients are determined from the measurement, the field can be evaluated on an arbitrary point in space as long as it is not within the MRE of the source.

A scenario which is frequently encountered in practice is the so called near-field to far-field transform where the near-field of the AUT is measured on a sphere and the far-field is desired. This task can easily be accomplished with the derivations above and is summarized in in the following list.

1. **Measuring:** The tangential field of the AUT is measured on a sphere with radius A surrounding the source. A probe with only first-order coefficients is used for the measurement.

2. **Analysis:** The spherical multipole coefficients Q_{smn} are calculated using Equation 47 - Equation 50.

3. **Synthesis:** The tangential field of the AUT is calculated on a sphere with radius A' surrounding the source.

Usually, the measurement radius A is in the near-field of the AUT and the synthesis radius A' is in the far-field. Then the above algorithm is referred to as a *near-field to far-field transform*. But the method is not restricted to this case. Measurement and synthesis radius are arbitrary as long as none of them is smaller than the MRE of the AUT.

$$20 \log |E_\theta|$$
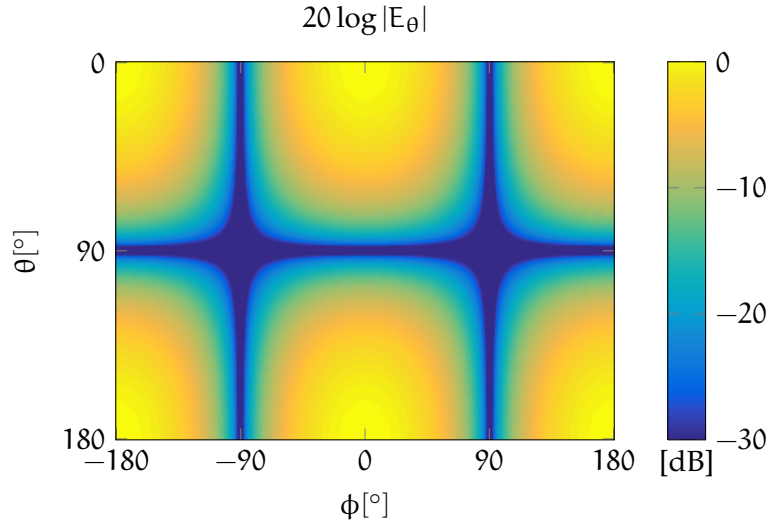
Figure 3: Logarithmic depiction of $|E_\theta|$ of a x-directed Hertzian dipole normalized to the maximum amplitude.

There exist very efficient algorithms for solving Equation 47 - Equation 50 based on the Fast Fourier Transform (FFT) Algorithm, but developing implementation specific formulations is out of the scope of this thesis. It is noted that for all calculations of the multipole coefficients and the far-field of antennas throughout this theses, a Matlab implementation was used.

2.3 THE HERTZIAN DIPOLE

To illustrate our results until now, we consider the simplest source of radiation, the Hertzian dipole. It is perfectly suitable to be our test case because the electric field as well as the multipole coefficients can be easily calculated. With the dipole moment **p**, the electric field of Hertzian dipole is written as (cf. [13])

$$\mathbf{E} = \frac{1}{4\pi\epsilon} \left[k^2 (\hat{\mathbf{r}} \times \mathbf{p}) \times \hat{\mathbf{r}} \frac{e^{ikr}}{r} + [3\hat{\mathbf{r}}(\hat{\mathbf{r}} \cdot \mathbf{p}) - \mathbf{p}] \left(\frac{1}{r^3} - \frac{ik}{r^2} \right) e^{ikr} \right] . \quad (51)$$

The point in space where the field is evaluated is denoted by **r** with the magnitude $r = |\mathbf{r}|$ and the vector of unit length $\hat{\mathbf{r}} = \mathbf{r}/r$.

Figure 3 shows the logarithmically scaled absolute value of the θ-component of the electric field, i.e. $E_\theta = \mathbf{E} \cdot \hat{\boldsymbol{\theta}}$, for a Hertzian dipole with the dipole moment **p** coinciding with the x-axis, i.e. $\mathbf{p} = p\hat{\mathbf{x}}$. The field amplitude is normalized to its maximum value. Figure 4 shows the absolute value of the corresponding ϕ-component E_ϕ.

The multipole coefficients Q_{smn} obtained by Equation 47 - Equation 50 are shown in Table 2 and Table 3. In the simple case of a Hertzian dipole, only modes of degree $n = 1$ are needed to fully characterize the source. All other coefficients are zero.
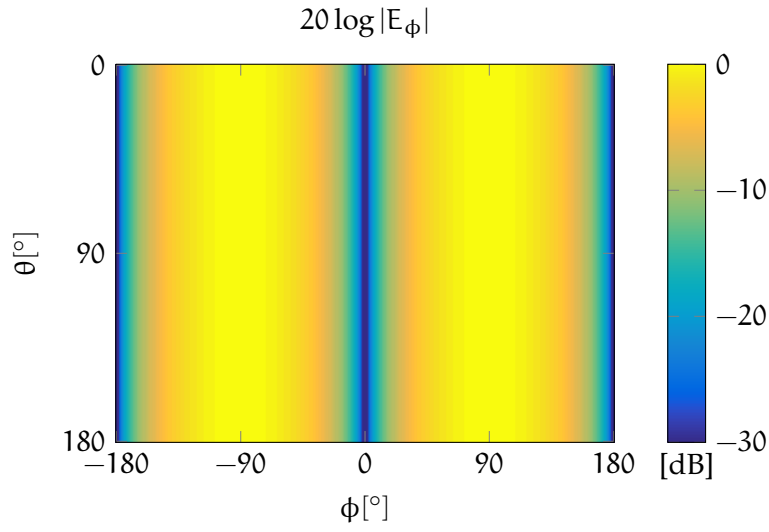
Figure 4: Logarithmic depiction of $|E_\phi|$ of a x-directed Hertzian dipole normalized to the maximum amplitude.

Table 2: Multipole coefficients Q_{1mn} of the x-directed Hertzian dipole normalized to unit transmit power $P = \frac{1}{2} \sum_{smn} |Q_{smn}|^2 = 1$.

$\mathbf{Q_{1mn}}$	$m = \pm 1$	$m = \pm 2$	$m = \pm 3$	...
$n = 1$	0	—	—	...
$n = 2$	0	0	—	...
$n = 3$	0	0	0	...
$\vdots$	$\vdots$	$\vdots$	$\vdots$	$\ddots$

Table 3: Multipole coefficients Q_{2mn} of the x-directed Hertzian dipole normalized to unit transmit power $P = \frac{1}{2} \sum_{smn} |Q_{smn}|^2 = 1$.

$\mathbf{Q_{2mn}}$	$m = \pm 1$	$m = \pm 2$	$m = \pm 3$	...
$n = 1$	$\mp i$	—	—	...
$n = 2$	0	0	—	...
$n = 3$	0	0	0	...
$\vdots$	$\vdots$	$\vdots$	$\vdots$	$\ddots$
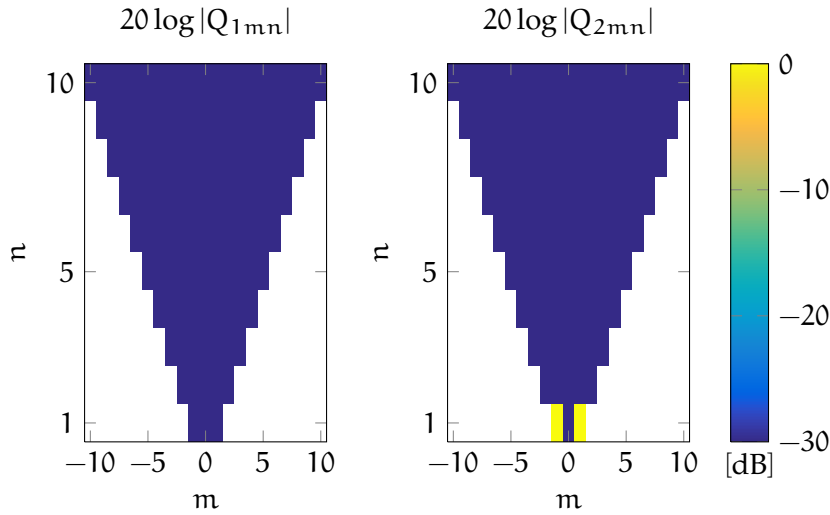
Figure 5: Logarithmic depiction of $|Q_{smn}|$ of a x-directed Hertzian dipole normalized to the maximum value.

An alternative way of depicting the multipole coefficients is shown in Figure 5. The data points for $m > n$ are left blank since only coefficients with $|m| \leqslant n$ are needed for the expansion in Equation 39. A cutoff degree of $N = 10$ according to Equation 38 was chosen.

2.3.1 *Shifting the Source*

In the previous section it was shown that for a Hertzian dipole, we only need multipole coefficients of degree $n = 1$ to fully characterize the source. This is only true if the dipole is located in the origin of the coordinate system. If the source is shifted outwards by the the vector $\mathbf{r}'$, then according to Equation 38 we need coefficients up to degree

$$N = \lceil k(r_0 + |\mathbf{r}'|) \rceil + 10 \tag{52}$$

to accurately describe the source. Figure 6 illustrates the distribution of transmit power over the modes n. For larger shifts $\mathbf{r}'$, modes with higher degree n contribute more to the total field. Therefore, a higher cutoff degree N is needed for an accurate description in terms of multipole coefficients.

The direction of shifting only effects the distribution of transmit power among order m modes for a fixed degree. Thus, the direction of shifting has no impact on the n-node power spectrum since the power of all modes with order m is summed up in Equation 36.

This fact has important implications for the next chapters. This is why Figure 7 gives a simplified overview of the power distribution among modes under translation and rotation. Simply put, a rotation redistributes power within one level of the "coefficient pyramid". The cutoff degree N is therefore not altered. A translation redistributes
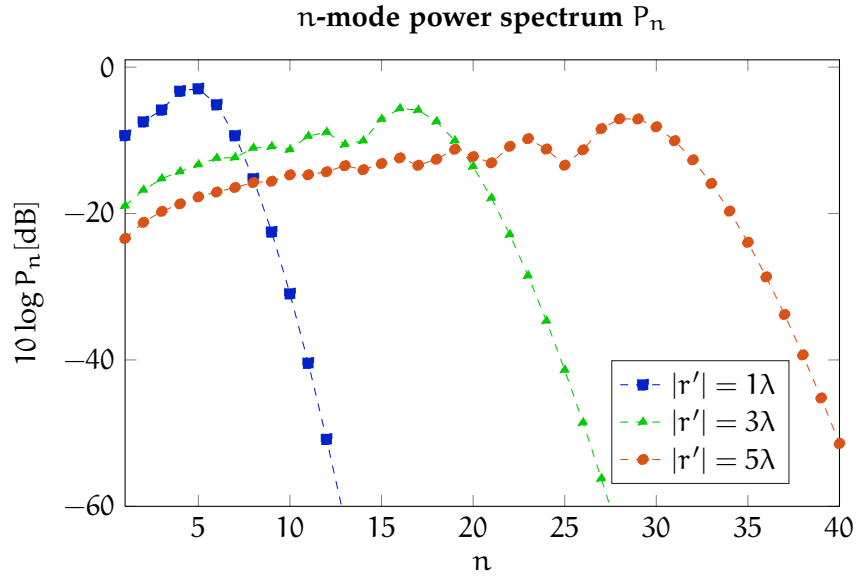
Figure 6: n-mode power spectrum P_n for different shifts from the coordinate origin $|\mathbf{r}'|$ normalized to the total radiated power P.

power among different levels of the "coefficient pyramid" and the cutoff degree has to be altered accordingly.

Calculating the new coefficients (i. e. after shifting) of a source using the old coefficients is computationally very expensive and numerically challenging. Fortunately, there is an easy approximation which leads to good results and is easy to obtain. For this we use the previously developed near-field to far-field transform to transform the tangential field of the source to the radius A'_{FF} in the far-field. There, we assume that a small shift $|\mathbf{r}'| \ll A'_{FF}$ only affects the *phase* of the field and the *amplitude* stays the same. By applying a phase correction term $E_{shift} = E e^{ik\hat{\mathbf{r}}\cdot\mathbf{r}'}$ and transforming the field back to the near-field the shifted field and its coefficients are known.

$$20 \log |Q_{smn}|$$
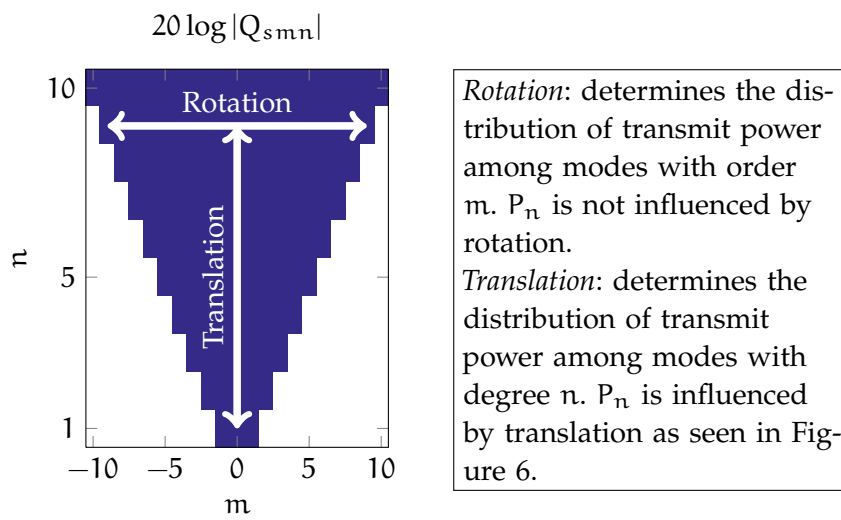
Figure 7: Depiction of the power distribution among modes under translation and rotation.

Rotation: determines the distribution of transmit power among modes with order m. P_n is not influenced by rotation.
Translation: determines the distribution of transmit power among modes with degree n. P_n is influenced by translation as seen in Figure 6.

PHASE CENTER AND ROTATIONAL SYMMETRY

One of the first applications of compressed sensing was reducing measurement time for MRI scans in medical applications as introduced in [12]. Sparsity of the measurement data in some domain can be exploited to allow for sampling rates far below the Nyquist rate (cf. [15]). Because of the similar measurement setup, these methods can readily be applied to antenna measurements. Before doing this, two new concepts have to be introduced which help applying compressed sensing techniques to antenna measurements, namely the phase center and the rotational symmetry of a source.

3.1 PHASE CENTER OF AN ANTENNA

In [16], the phase center of an antenna is defined as follows:

> **2.270 phase center**. The location of a point associated with an antenna such that, if it is taken as the center of a sphere whose radius extends into the far-field, the phase of a given field component over the surface of the radiation sphere is essentially constant, at least over that portion of the surface where the radiation is significant.

For all practical antennas the phase center is not uniquely defined. Its position depends on the angle of observation, the frequency, the polarization and the considered angular space. Often it is possible to find a point for which the phase is nearly constant over a reasonable angular space. Following [17], this point is then referred to as the apparent phase center. The importance of the phase center becomes clear when a paraboloidal reflector antenna is considered. The feed antenna has to be mounted in a way that its phase center coincides with the focal point of the paraboloid. Otherwise significant performance degradations are introduced.

In what follows, a new method for phase center determination is introduced and its performance is compared to the LS procedure which is the standard method for phase center determination in antenna theory (cf. [5, 6, 7]). The new method uses a 1-norm minimization of the spherical multipole coefficients to estimate the phase center and proves to be superior in terms of precision and reliability. But before going into details, a matrix vector notation is introduced for the spherical multipole expansion. This helps keeping a clean and concise notation throughout the following chapters.

3.1.1 *Matrix Notation*

The simplified transmission formula from Equation 45 reads as

$$w(A, \chi, \theta, \phi) = \sum_{\substack{smn \\ \mu}} Q_{smn} e^{im\phi} d^n_{\mu m}(\theta) e^{i\mu\chi} P_{s\mu n}(kA) . \qquad (53)$$

Following the conventions from [1], a new summation index j is introduced which replaces the indices s, n and m. The new index

$$j = 2(n(n+1) + m - 1) + s \qquad (54)$$

simplifies the summation in the transmission formula to

$$\sum_{s=1}^{2} \sum_{n=1}^{N} \sum_{m=-n}^{n} = \sum_{j=1}^{J} \qquad (55)$$

with the new truncation index

$$J = 2N(N+2) . \qquad (56)$$

The inverse mapping to retain the old indices can be calculated easily via a three step algorithm:

$$s(j) = j_s = (j - 1 \mod 2) + 1$$

$$n(j) = j_n = \left\lfloor \sqrt{\frac{j - j_s}{2} + 1} \right\rfloor \qquad (57)$$

$$m(j) = j_m = \frac{j - j_s}{2} + 1 - j_n(j_n + 1) .$$

Figure 8 shows the mapping from old to new index set.
   The transmission formula can now be written as

$$w(A, \chi, \theta, \phi) = \sum_{j=1}^{J} \sum_{\mu} Q_j e^{ij_m\phi} d^{j_n}_{\mu j_m}(\theta) e^{i\mu\chi} P_{j_s\mu j_n}(kA) , \qquad (58)$$

which can be condensed into a compact matrix form

$$w = FQ \qquad (59)$$

with the matrices

$$(w)_l = w(A, \chi_l, \theta_l, \phi_l) \qquad (60)$$

$$(Q)_j = Q_j = Q_{j_s j_m j_n} \qquad (61)$$

$$(F)_{l,j} = \sum_{\mu} e^{ij_m\phi_l} d^{j_n}_{\mu j_m}(\theta_l) e^{i\mu\chi_l} P_{j_s\mu j_n}(kA) \qquad (62)$$

$$w \in \mathbb{C}^{L\times 1} \qquad (63)$$

$$F \in \mathbb{C}^{L\times J} \qquad (64)$$

$$Q \in \mathbb{C}^{J\times 1} \qquad (65)$$

$$\qquad (66)$$
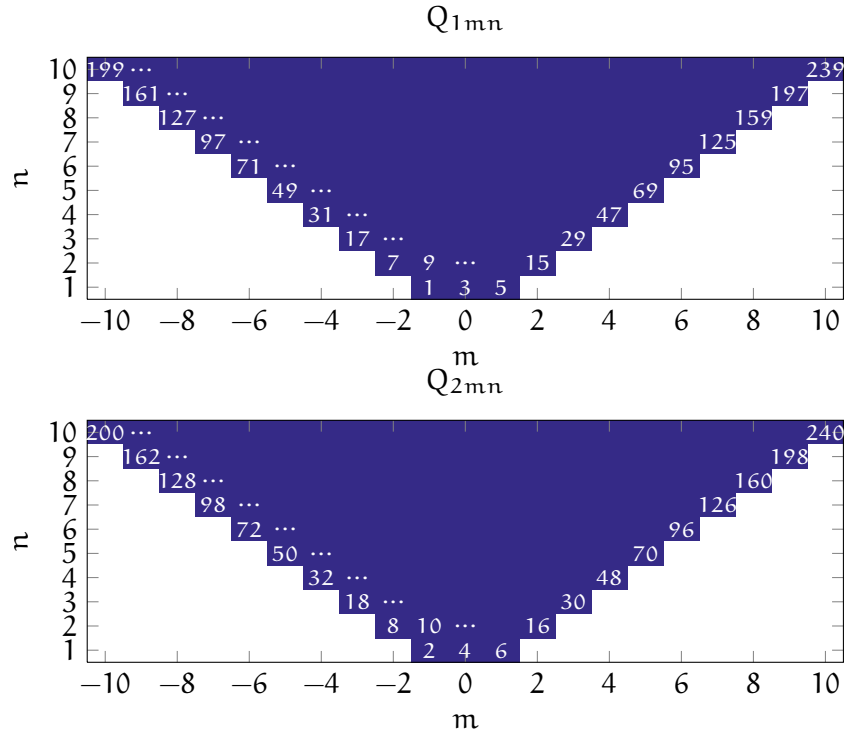
Figure 8: Depiction of the index mapping $(s, m, n) \rightarrow j$. The new j index (white) is placed at its corresponding position (s, m, n) in the coefficient pyramid.

and the measurement index $l = 1, \ldots, L$. The new index j provides means to organize the index triplet (s, m, n) into a single vector, as can be seen in the coefficient matrix (cf. Figure 8)

$$\mathbf{Q} = \begin{pmatrix} Q_1 \\ Q_2 \\ Q_3 \\ \vdots \\ Q_{J-1} \\ Q_J \end{pmatrix} = \begin{pmatrix} Q_{1,-1,1} \\ Q_{2,-1,1} \\ Q_{1,0,1} \\ \vdots \\ Q_{1,N,N} \\ Q_{2,N,N} \end{pmatrix}. \tag{67}$$

Equation 59 implies that if $L = J$ independent measurements are taken, the multipole coefficient matrix $\mathbf{Q}$ can be calculated by inversion of $\mathbf{F}$. In practice the coefficients are never calculated by simple inversion because of its numerical instability. Other methods which use a Fourier representation of $\mathbf{F}$ are used instead. Nevertheless, the notation

$$\mathbf{Q} = \mathbf{F}^{-1} \boldsymbol{w} \tag{68}$$

will be used to denote the calculation of the coefficients $\mathbf{Q}$. To summarize, the near-field to far-field transform algorithm outlined in Section 2.2.2 can be compactly written as

$$w_{\mathrm{FF}} = \mathbf{F}_{\mathrm{FF}} \underbrace{\mathbf{F}_{\mathrm{NF}}^{-1} w_{\mathrm{NF}}}_{\mathbf{Q}}, \tag{69}$$

where the subscripts $(\cdot)_{\mathrm{NF}}$ and $(\cdot)_{\mathrm{FF}}$ indicate if the analysis and synthesis radius A of the respective quantity lies in the near-field or far-field.

In Section 2.3.1 the translation operation for the far-field of a source is introduced. This operation can be compactly written in terms of the matrix notation. The shifted multipole coefficients $\mathbf{Q}_{\mathrm{shift}}$ are obtained as

$$\mathbf{Q}_{\mathrm{shift}} = \mathbf{F}_{\mathrm{FF}}^{-1} \tilde{\mathbf{T}} \mathbf{F}_{\mathrm{FF}} \mathbf{Q} = \mathbf{T} \mathbf{Q} \tag{70}$$

with the far-field translation matrix $\tilde{\mathbf{T}}$ defined as

$$\tilde{\mathbf{T}}(\mathbf{r}') = \begin{bmatrix} e^{ik\hat{\mathbf{r}}_1 \cdot \mathbf{r}'} & 0 & \cdots & 0 \\ 0 & e^{ik\hat{\mathbf{r}}_2 \cdot \mathbf{r}'} & \ddots & \vdots \\ \vdots & \ddots & \ddots & 0 \\ 0 & \cdots & 0 & e^{ik\hat{\mathbf{r}}_L \cdot \mathbf{r}'} \end{bmatrix} \in \mathbb{C}^{L \times L}. \tag{71}$$

The phase correction factors in the diagonal of $\tilde{\mathbf{T}}$ are constituted of the inner product of the unit vector $\hat{\mathbf{r}}_l$ pointing in the direction of the lth measurement and the shifting vector $\mathbf{r}'$ scaled by the wavenumber k.

Similar to the translation matrix $\mathbf{T}$, a rotation matrix $\mathbf{R} \in \mathbb{C}^{J \times J}$ is used to carry out a rotation of the field by the three Euler angles (χ, θ, ϕ). For the rotation sequence, the (z, y, z)-convention is used. Rotation of the coordinate system as derived in [1, Chapter 3] leads to a sum invoking the rotation angles and the rotation coefficient introduced in Section 2.2.2

$$Q_{smn,\mathrm{rotate}} = \sum_{\mu=-n}^{n} e^{im\phi} d_{\mu m}^{n}(\theta) e^{i\mu\chi} Q_{s\mu n}. \tag{72}$$

By using the new indices j and l (Equation 54) and writing the μ-sum as a matrix multiplication, the rotated coefficients $\mathbf{Q}_{\mathrm{rotate}}$ are calculated by

$$\mathbf{Q}_{\mathrm{rotate}} = \mathbf{R} \mathbf{Q} \tag{73}$$

with

$$(\mathbf{R})_{j,l}(\chi, \theta, \phi) = \begin{cases} e^{ij_m\phi} d_{l_m j_m}^{j_n}(\theta) e^{il_m\chi} & l \in \mathcal{L}(j) \\ 0 & \text{otherwise} \end{cases} \tag{74}$$

and the set of admissible values for l (which depends on the current j index)

$$\mathcal{L}(j) = \big\{ l : \quad l = 2\big(j_n(j_n + 1) + \mu - 1\big) + j_s, \\ \mu \in \{-j_n, -j_n + 1, \ldots, j_n\} \big\}. \tag{75}$$

3.1.2 *Minimum 1-Norm Estimation*

In Section 2.3.1 (Figure 6 and Figure 7 in particular) the effects of translating a source relative to the coordinate origin are shown. For larger distances between origin and source the modal content is shifted towards modes with higher degree n. On the contrary, if the sources n-mode power spectrum is concentrated on lower degree modes, this implies relative closeness of source and coordinate origin. It is therefore save to assume that if the n-mode power spectrum is "maximally focused" (in a sense which is still to be defined) on low degrees, the coordinate origin coincides with the phase center of the source.

Another way of establishing this issue is the analogy with the Fourier transform where the mode degree n takes over the role of the frequency. To ensure a slowly varying phase, only low frequency components should be present. Constant phase as suggested for the phase center by [16] is guaranteed if only the DC-component of the Fourier transform is present.

PHASE CENTER DEFINITION   The explanations above motivate the following definition. The phase center of a source is the point for which $\mathbf{Q}_{\text{shift}}$ has the fewest non-zero entries. In mathematical terms the phase center is defined as

$$\begin{aligned} \mathbf{r}_{\text{PC}} &= -\arg\min_{\substack{\mathbf{r}' \\ r' < r_0}} \|\mathbf{Q}_{\text{shift}}\|_0 \\ &= -\arg\min_{\substack{\mathbf{r}' \\ r' < r_0}} \|\mathbf{F}_{\text{FF}}^{-1}\tilde{\mathbf{T}}(\mathbf{r}')\mathbf{F}_{\text{FF}}\mathbf{Q}\|_0 \end{aligned} \tag{76}$$

with r_0 being the MRE of the source. As usual, the p-norm of a vector $\mathbf{x}$ is defined as

$$\|\mathbf{x}\|_p = \left(\sum_i |x_i|^p \right)^{\frac{1}{p}}, \quad p \geqslant 1. \tag{77}$$

This expression can be extended to smaller values $0 < p < 1$, but due to the violation of the triangle inequality it does not constitute a

proper norm. The case $p = 0$ and the corresponding quasi-norm $\|\mathbf{x}\|_0$ denote the number of non-zero elements of $\mathbf{x}$, i. e.

$$\|\mathbf{x}\|_0 = \sum_i I(x_i) \tag{78}$$

$$I(x_i) = \begin{cases} 1 & x_i \neq 0 \\ 0 & x_i = 0 \end{cases}. \tag{79}$$

It is important to note that the cutoff index J up to which the multipole coefficients $\mathbf{Q}$ are calculated has to be chosen large enough. Otherwise, a shift might redistribute power contributions to indices larger than the cutoff index which entails false minimization results in Equation 76. Moreover, the absolute value r' of the shift vector needs to be smaller than r_0 (which is the MRE of the source).

Equation 76 requires a combinatorial search over all possible values for the shift vector $\mathbf{r}'$ and is therefore not suitable for standard optimization routines. The solution to this problem is the utilization of the 1-norm in the argument of the minimization. It is shown in [15] that this step renders the optimization problem convex while maintaining the sparsity constraint on $\mathbf{Q}_{\text{shift}}$. The definition of the phase center then reads as

$$\begin{aligned} \mathbf{r}_{\text{PC}} &= -\arg\min_{\substack{\mathbf{r}' \\ r' < r_0}} \|\mathbf{Q}_{\text{shift}}\|_1 \\ &= -\arg\min_{\substack{\mathbf{r}' \\ r' < r_0}} \|\mathbf{F}_{\text{FF}}^{-1} \tilde{\mathbf{T}}(\mathbf{r}') \mathbf{F}_{\text{FF}} \mathbf{Q}\|_1 \end{aligned} \tag{80}$$

and allows for a simple implementation.

SIMULATION RESULTS   A broadly established and straightforward way of calculating the phase center of an antenna is to compare the measured field of an antenna with the theoretic field of a point source and translate the antenna so that an error term becomes minimal in an LS sense. For further details and implementation guidelines, the reader is referred to [5]. The algorithm found there is frequently applied in practice and will be the benchmark the new algorithm is compared to.

For simulation purposes, the field of an electric dipole is calculated according to Equation 51 with random dipole moment $\mathbf{p}$ and random shift $\mathbf{r}'$ with magnitude smaller than one wavelength. The error vector is then calculated by

$$\mathbf{r}_e = \mathbf{r}_{\text{PC}} + \mathbf{r}' \tag{81}$$

and its length

$$r_e = \|\mathbf{r}_e\|_2 \tag{82}$$
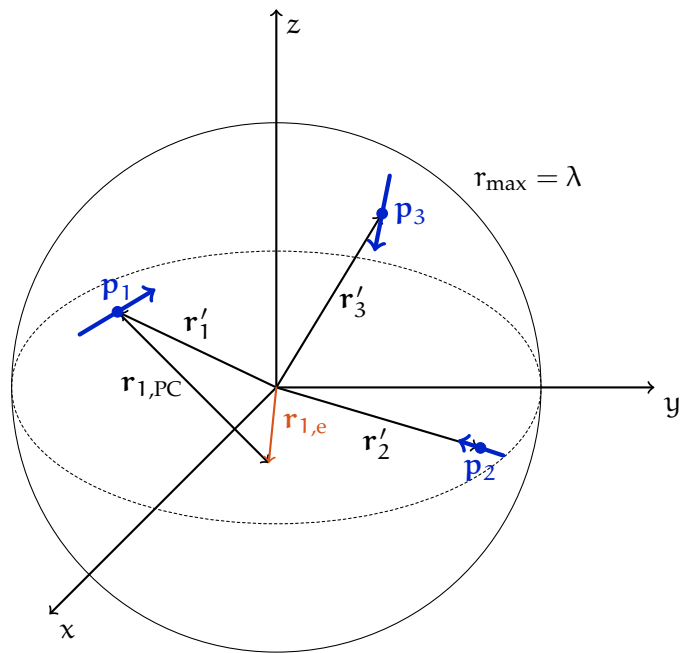
Figure 9: Simulation Setup for comparison of phase center detection perfor-
mance based on an LS method and the minimum 1-norm method
from Equation 80. The dipole moments $\mathbf{p}_i$ (blue) are chosen with
random orientation and magnitude. The corresponding fields are
calculated and then shifted by respective random vectors $\mathbf{r}'_i$. The
error vector $\mathbf{r}_{i,e}$ (orange) and its magnitude are used as perfor-
mance metric.

is used as a performance metric to evaluate the precision of the two proposed phase center detection techniques. Figure 9 illustrates the measurement setup.

To carry out the minimization in Equation 80, the Sequential Quadratic Programming (SQP) solver of the Matlab function `fmincon` is used. The step size tolerance is set to $\lambda/1000$ and a random starting point within a sphere of radius λ is chosen.

Figure 10 shows the results for $M = 1000$ measurements. The performance of the LS-based phase center detection depends on the orientation of the dipole moment. Since the moment $\mathbf{p}_i$ was chosen at random, there is a large fluctuation in the achieved precision. Further, it seems that offsets in the z-direction can be better compensated than offsets in the x- or y-direction. This is caused by the higher sampling density in the polar regions of the measurement sphere. The minimum 1-norm does not exhibit dependencies on the orientation or the offset direction. Translations are estimated very precisely and robustly. In some part this is due to the fact that a dipole has the smallest norm $\|\mathbf{Q}\|_1$ possible for a given transmit power $\frac{1}{2}\|\mathbf{Q}\|_2$. This is of course a favorable scenario for the minimization problem. But nevertheless, the method works equally well for all different kinds of sources since the underlying principle is the same for all antennas.

Table 4 summarizes the simulation results. The quantities used for the performance evaluation are the sample mean of the absolute error

$$\bar{r}_e = \frac{1}{M} \sum_{i=1}^{M} r_{i,e} \, , \tag{83}$$

the unbiased sample standard deviation

$$s = \sqrt{\frac{1}{M-1} \sum_{i=1}^{M} (r_{i,e} - \bar{r}_e)^2} \, , \tag{84}$$

the radius which is larger than 95% of all absolute error radii

$$r_{e,95\%} = \min_r r \quad \text{s.t.} \quad P\{r_{i,e} < r\} \geqslant 0.95 \, , \tag{85}$$

the maximum of the absolute error

$$r_{e,\max} = \max_i r_{i,e} \, , \tag{86}$$

and the sample mean of the execution time

$$\bar{t} = \frac{1}{M} \sum_{i=1}^{M} t_i \, . \tag{87}$$

It is obvious from the results in Table 4 that the minimum 1-norm estimation provides superior accuracy and reliability. This gain is
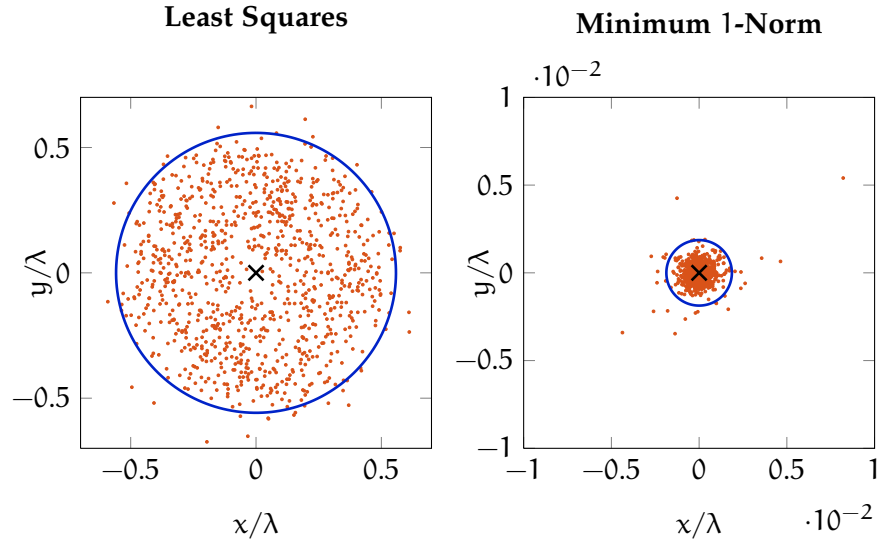
(a) Error distribution in xy-plane for LS-method

(b) Error distribution in xy-plane for minimum 1-norm method
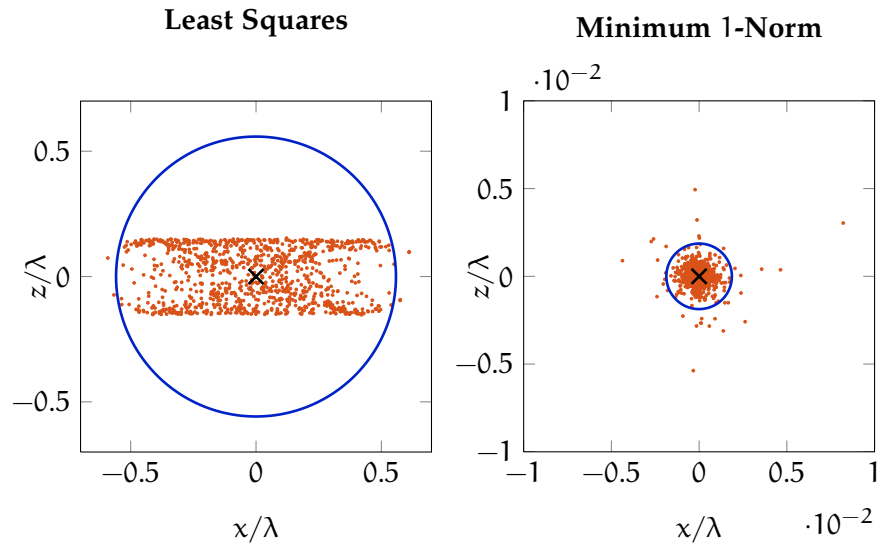
(c) Error distribution in xz-plane for LS-method

(d) Error distribution in xz-plane for minimum 1-norm method

Figure 10: The distribution of error vectors $\mathbf{r}_{i,e} = \mathbf{r}_{i,PC} + \mathbf{r}'_i$ (see Figure 9) is shown for the two considered phase center detection methods in the xy-plane and in the xz-plane. Each error vector $\mathbf{r}_{i,e}$, $i = 1, \ldots, M$ is indicated by an orange dot. For perfect estimation it holds that $\mathbf{r}_{i,e} = 0$ (black cross). The sphere with radius $r_{e,95\%}$ containing 95% of the simulation results for the respective method is indicated in blue. The minimum 1-norm method is more accurate (note the different scaling of the axes) and not dependent on orientation.

Table 4: Comparison of the LS- and the minimum 1-norm based phase center detection methods. The simulation was carried out $M = 1000$ times. The minimum 1-norm method provides superior precision but is more computationally expensive. The maximum error is larger since in some rare cases, the Matlab optimization does not converge.

Method:	Least Squares	Minimum 1-Norm
$\bar{r}_e$	$372.60 \cdot 10^{-3}\lambda$	$1.81 \cdot 10^{-3}\lambda$
s	$125.76 \cdot 10^{-3}\lambda$	$29.05 \cdot 10^{-3}\lambda$
$r_{e,95\%}$	$558.32 \cdot 10^{-3}\lambda$	$1.87 \cdot 10^{-3}\lambda$
$r_{e,max}$	0.70λ	0.92λ
$\bar{t}$	$11.66 \cdot 10^{-3}s$	$8.31s$

bought by longer execution times. It has to be noted, however, that the routines for calculating the minimum 1-norm estimation have not been optimized for computation time. If execution time turns out to be a limiting factor for the use of this method, it can certainly be reduced significantly by an optimized implementation. This is, however, out of the scope of this thesis. The gain in precision over the conventional LS-method turns out to be a crucial component for reducing overall measurement time in antenna measurements. It is therefore acceptable to spend a little extra time on the phase center detection when measurement time can be reduced overall. These issues will be discussed in detail in the next chapters. The larger maximum error $r_{e,max}$ arises from a failed minimization in Equation 80. The iteration limit was reached without finding the global minimum. Preventing this case and increasing overall performance is possible by using the LS solution as starting point for the minimum 1-norm method and by checking if the phase variation is indeed minimal for the calculated phase center.

3.2 ROTATIONAL SYMMETRY OF AN ANTENNA

The notion of rotational symmetry for a given source is discussed next. The phase center was defined as the point in space for which, when coinciding with the coordinate origin, the multipole coefficients **Q** were "maximally focused" on modes with low degree n. In a similar manner, rotational symmetry is achieved when, after rotating the source by the Euler angles (χ, θ, ϕ), the multipole coefficients **Q** are "maximally focused" on modes with low order m.

The use of this definition will become clearer in the next chapters when the notion of compressed sensing is introduced. There, a sparse vector **Q** will lead to a reduction in necessary antenna measurement samples. The calculation of the multipole coefficients in an optimal

coordinate system (with the origin in the phase center and the z-axis as the axis of rotational symmetry) ensures the sparsest representation of $\mathbf{Q}$ possible.

3.2.1 *Minimum 1-Norm Estimation*

ROTATIONAL SYMMETRY DEFINITION   Similar to the phase center, the Euler angles necessary to achieve rotational symmetry are defined as rotation angles for which $\mathbf{Q}_{\text{rotate}}$ has the fewest non-zero entries. In mathematical terms, this reads as

$$
\begin{aligned}
(\chi, \theta, \phi)_{\text{RS}} &= \arg \min_{(\chi, \theta, \phi)} \|\mathbf{Q}_{\text{rotate}}\|_0 \\
&= \arg \min_{(\chi, \theta, \phi)} \|\mathbf{R}(\chi, \theta, \phi)\mathbf{Q}\|_0 \, .
\end{aligned}
\tag{88}
$$

Again, since optimization problems of the form Equation 88 are computationally intractable, a 1-norm relaxation is introduced to render the optimization problem tractable. The Euler angles to achieve rotational symmetry are then written as

$$
\begin{aligned}
(\chi, \theta, \phi)_{\text{RS}} &= \arg \min_{(\chi, \theta, \phi)} \|\mathbf{Q}_{\text{rotate}}\|_1 \\
&= \arg \min_{(\chi, \theta, \phi)} \|\mathbf{R}(\chi, \theta, \phi)\mathbf{Q}\|_1
\end{aligned}
\tag{89}
$$

and can be calculated using standard minimization techniques.

Figure 11 shows the effects of a rotation according to Equation 89 and a translation according to Equation 80 on the coefficients of a Hertzian dipole. Depending on the position and orientation of the source, a different number of non-zero entries in $\mathbf{Q}$ is necessary to accurately describe it in terms of multipole coefficients. Figure 11a shows to original position $\mathbf{r}$ and the dipole moment $\mathbf{p}$ while Figure 11b depicts the corresponding coefficients. Next, the coefficients $\mathbf{Q}' = \mathbf{R}\mathbf{Q}$ are rotated (cf. Figure 11c, Figure 11d). The necessary rotation angles are calculated using Equation 89. As a final step, the source is translated to the coordinate origin by $\mathbf{Q}'' = \mathbf{T}\mathbf{Q}' = \mathbf{T}\mathbf{R}\mathbf{Q}$ (cf. Figure 11e, Figure 11f). The necessary translation vector is calculated using Equation 80. With this approach a sparse representation of the source in terms of multipole coefficients is obtained.
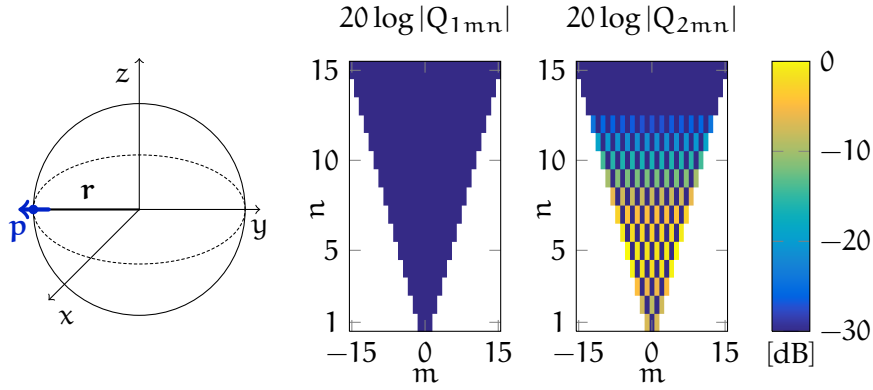
(a) Original position and orientation

(b) Original Coefficients
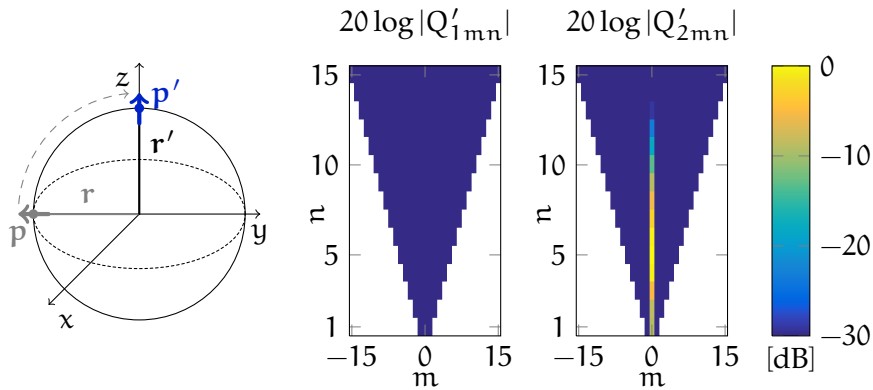
(c) Position and orientation after rotation by $(\chi, \theta, \phi)_{RS}$

(d) Coefficients after rotation by $(\chi, \theta, \phi)_{RS}$
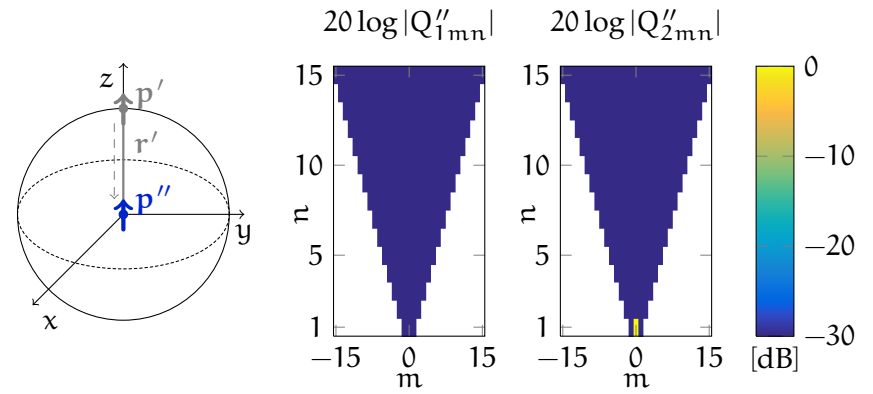
(e) Position and orientation after rotation by $(\chi, \theta, \phi)_{RS}$ and translation by $\mathbf{r}_{PC}$

(f) Coefficients after rotation by $(\chi, \theta, \phi)_{RS}$ and translation by $\mathbf{r}_{PC}$

Figure 11: The first row shows the position $\mathbf{r}$ (black) and orientation $\mathbf{p}$ (blue) of a Hertzian dipole and its corresponding multipole coefficients Q_{smn}. The second row shows the position, orientation and coefficients after a rotation, and successively, the third row shows the respective quantities after a translation.

COMPRESSED SENSING FOR ANTENNA MEASUREMENTS

The field of compressed sensing has been and still is a very active research area. The prospect of reducing the number of samples necessary to characterize a signal source has found great appeal in many applications. One of the very first usages of compressed sensing was the reduction of measurement time in MRI scans as described in [12]. Here, sparsity in the total variation of medical images is exploited so that the number of samples in the frequency domain decreases. The similarity of this setup to antenna measurements is one of the main inspirations for this thesis. Later we will see how compressed sensing can be applied to antenna characterization. But before, the basic principles and results of sparse signal recovery are introduced.

4.1 RECOVERY OF SPARSE SIGNALS

Suppose we have an arbitrary discrete signal $f(n)$ of size N which is non-zero only on a subset $T \subseteq \{0, 1, \ldots N - 1\} = \mathbb{Z}_N$. The support size of f is thus

$$|\text{supp}(f)| = |T| = \sum_{n=0}^{N-1} I(f(n)) \tag{90}$$

with the indicator function $I(x)$ (Equation 79) being 1 for non-zero entries of x and zero else. The discrete Fourier transform of the sequence is defined as

$$\hat{f}(k) = \sum_{n=0}^{N-1} f(n)e^{-i\frac{2\pi kn}{N}} = \sum_{n=0}^{N-1} f(n)e^{-i\omega_k n} \tag{91}$$

and its inverse reads as

$$f(n) = \frac{1}{N} \sum_{k=0}^{N-1} \hat{f}(k)e^{i\omega_k n} . \tag{92}$$

Similar to Equation 90, the support size of $\hat{f}$ is defined as

$$|\text{supp}(\hat{f})| = |\Omega| = \sum_{k=0}^{N-1} I(\hat{f}(k)) \tag{93}$$

with the support $\Omega \subseteq \mathbb{Z}_N$ being the subset on which $\hat{f}$ is non-zero.

If all entries of $\hat{f}(k)$, $k = 0, 1, \ldots, N - 1$ are known, the signal $f(n)$ can simply be reconstructed using the inverse Fourier transform from

Equation 92. In the well known paper [9] it is shown that we can do significantly better if $f(n)$ is supported only on a small subset T, i.e. if $f(n)$ is sparse. Then it suffices to know $\hat{f}(k)$ on a subset Ω satisfying

$$|T| \leqslant \frac{1}{2}|\Omega| \tag{94}$$

to guarantee (for N prime) exact reconstruction of $f(n)$ from the limited number of frequency samples $\hat{f}(k), k \in \Omega$. The algorithm achieving exact reconstruction is a combinatorial search, i.e.

$$(P_0) \qquad \min_g \|g\|_0 \quad \text{s.t.} \quad \hat{g}(k) = \hat{f}(k), \ k \in \Omega . \tag{95}$$

Solving this optimization problem directly is not feasible due to its combinatorial complexity. Therefore, the following relaxation is introduced

$$(P_1) \qquad \min_g \|g\|_1 \quad \text{s.t.} \quad \hat{g}(k) = \hat{f}(k), \ k \in \Omega \tag{96}$$

which can be solved numerically in a very efficient manner. The remarkable observation proved in [9] is that (P_0) and (P_1) are equivalent for almost all choices of Ω given that

$$|T| \leqslant \frac{\alpha|\Omega|}{\log N} . \tag{97}$$

To underline the significance of this result, let us consider a small example. To reconstruct a time signal $f(n)$ of length $N = 1000$ from its Fourier coefficients via Equation 92, we need all of its Fourier coefficients $\hat{f}(k)$, $k = 0, \ldots, 999$. If we know that the support $|T|$ of $f(n)$ is 10, i.e. $f(n)$ is non-zero on 10 unknown positions, numerical results in [9] suggest that 100 random samples of $\hat{f}(k)$ are enough to recover the signal $f(n)$ exactly with probability almost 1.

The methodology introduced above only considers the case of sampled Fourier coefficients and cannot be directly related to the spherical coefficients domain. However, subsequent work of the afore mentioned authors extends the compressed sensing framework to a larger set of transform pairs.

UNIFORM UNCERTAINTY PRINCIPLE DEFINITION   To verify if a given transform pair is suitable for a compressed sensing approach, the notion of the Uniform Uncertainty Principle (UUP) is introduced [11, 18]. Assume F_Ω is an $|\Omega| \times N$ matrix (often called the sensing matrix) and $\hat{f} = F_\Omega f$. The matrix F_Ω fulfills the UUP with S-restricted isometry constant δ_S if the inequality

$$(1 - \delta_S)\|f\|_2^2 \leqslant \|F_\Omega f\|_2^2 \leqslant (1 + \delta_S)\|f\|_2^2 \tag{98}$$

holds for all subsets T with $|T| \leqslant S$ and $\text{supp}(f) = T$. Essentially, Equation 98 states that the samples $\hat{f} = F_\Omega f$ capture a "fair share"

of the signal energy and that the power which is not captured is bounded by δ_S. According to [18], "This property essentially requires that every set of columns with cardinality less than S approximately behaves like an orthonormal system."

In general, it is very hard to prove if an arbitrary sensing matrix fulfills the UUP with good isometry constants. Numerical evaluation fails since the number of different supporting subsets T and the number of different sampling subsets Ω is to large for an exhaustive search. However, randomness in the sensing matrices allows for probabilistic statements concerning uniform uncertainty and sparsity $S = |T|$. Sensing matrices F_Ω often encountered in literature are [10, 11]

- *The Gaussian sensing matrix:* The entries of $F_\Omega \in \mathbb{R}^{|\Omega| \times N}$ are sampled from a normal distribution

$$(F_\Omega)_{k,n} = \frac{1}{\sqrt{N}} X_{k,n}, \quad X_{k,n} \text{ i.i.d. } N(0,1). \tag{99}$$

  The UUP is satisfied with probability $1 - \mathcal{O}(e^{-\gamma N})$, $\gamma > 0$ if

$$S \leqslant \frac{\alpha |\Omega|}{\log \frac{N}{|\Omega|}}. \tag{100}$$

- *The binary sensing matrix:* The entries of $F_\Omega \in \mathbb{R}^{|\Omega| \times N}$ are sampled from a symmetric Bernoulli distribution

$$(F_\Omega)_{k,n} = \frac{1}{\sqrt{N}} X_{k,n}, \quad P\{X_{k,n} = \pm 1\} = 0.5. \tag{101}$$

  The UUP is satisfied with probability $1 - \mathcal{O}(e^{-\gamma N})$, $\gamma > 0$ if

$$S \leqslant \frac{\alpha |\Omega|}{\log \frac{N}{|\Omega|}}. \tag{102}$$

- *The Fourier sensing matrix:* The entries of $F_\Omega \in \mathbb{C}^{|\Omega| \times N}$ are obtained by randomly choosing $|\Omega|$ rows from an orthonormal Fourier matrix

$$(F_\Omega)_{k,n} = \frac{1}{\sqrt{N}} e^{-i2\pi \frac{kn}{N}}, \quad k \in \Omega, \ n = 1, \dots, N \tag{103}$$

  The UUP is satisfied with probability $1 - \mathcal{O}(e^{-\gamma N})$, $\gamma > 0$ if

$$S \leqslant \frac{\alpha |\Omega|}{(\log N)^6}. \tag{104}$$

To get an intuitive idea of the UUP, a visualization is quite helpful. Consider a Fourier sensing matrix as defined in Equation 103. A signal f with spikes on just a few positions and zeros otherwise (Figure 12a) is known to have a rich spectrum to capture the sharp transitions. Its Fourier transform $\hat{f}$ has therefore necessarily a large support accounting for the high frequency components introduced by the

sharp transitions (Figure 12b). If now the Fourier domain is sampled on a random subset Ω, the probability to capture a "fair share" of power is quite large. But the larger the support $|T|$ of f becomes, the more concentrated the spectrum might be. This results in reduced probability of fulfilling the UUP with good isometry constants. Vice versa, if the Fourier transform has only a few distinct frequency components (Figure 12d), the corresponding time signal can never be localized in time (Figure 12c). Summarizing this example, a sensing matrix F_Ω satisfying the UUP guarantees that a signal f in the original domain and a signal $\hat{f} = F_\Omega f$ in the transform domain can never be sparse at the same time.
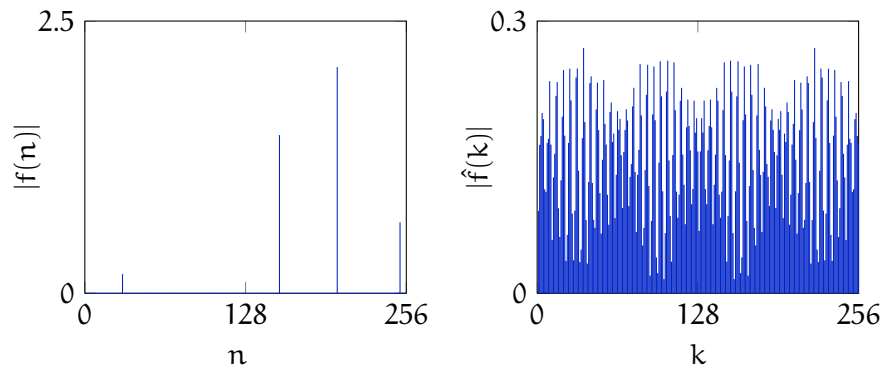
(a) Signal $f(n)$ is highly localized in time ...

(b) ...but its Fourier transform $\hat{f}$ is distributed over frequency.
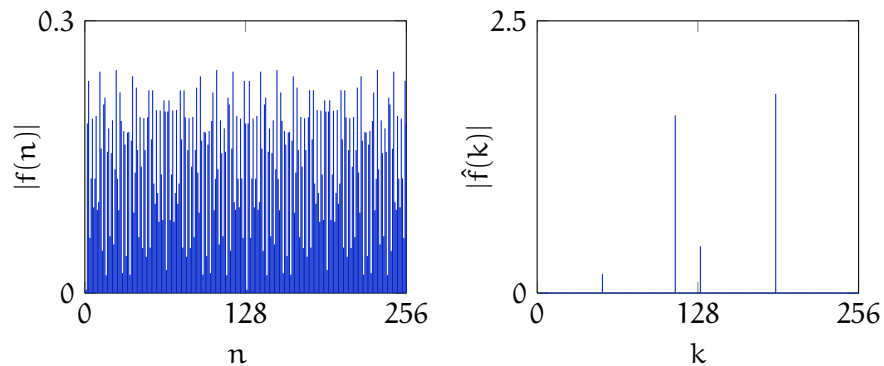
(c) Signal $f(n)$ is distributed over time ...

(d) ...but its Fourier transform $\hat{f}$ is localized in frequency.

Figure 12: Visualization of the UUP for Fourier matrices. Signals which are highly localized in time have a broad frequency spectrum (first row). On the contrary, signals with just a few frequency components do not have sparse time support (second row).

The UUP and accordingly the isometry constant δ_S can now be used to derive statements for signal recovery and stability using the recovery algorithms stated in Equation 95 and Equation 96.

In [10] it is shown that for

$$\delta_S + \delta_{2S} + \delta_{3S} \leqslant 1 \tag{105}$$

the program (P_1) recovers any sparse signal f satisfying $|T| \leqslant S$. Moreover, since the samples $\hat{f}$ are often not known exactly, a third recovery algorithm is introduced which amounts for small errors e,

$$(P_2) \qquad \min_{g \in \mathbb{C}^N} \|g\|_1 \quad \text{s.t.} \quad \|F_\Omega g - \hat{f}\|_2 = \|e\|_2 \leqslant \epsilon . \tag{106}$$

Equation 106 allows for reconstruction of the signal f with error constraint. In [10] it is proved that a solution $f^\sharp$ to (P_2) stays close to the original signal f with support size $|T| \leqslant S$,

$$\|f^\sharp - f\|_2 \leqslant C_S \epsilon, \tag{107}$$

given that

$$\delta_{3S} + 3\delta_{4S} \leqslant 2 \tag{108}$$

for a small constant C_S and error constraint $\|F_\Omega g - \hat{f}\|_2 = \|e\|_2 \leqslant \epsilon$. Under the same conditions as above,

$$\|f^\sharp - f\|_2 \leqslant C_{1,S} \epsilon + C_{2,S} \frac{\|f - f_S\|_1}{\sqrt{S}} \tag{109}$$

holds for an arbitrary signal f. The signal f_S is obtained by considering only the S largest entries of f and setting all other entries to zero. This result implies that if the isometry constants of a sampling matrix obeys certain constraints, the reconstruction error is subject to the sampling error constraint $\|e\|_2$ and by the term $\|f - f_S\|_1$ accounting for the non-sparseness of f.

4.2 APPLICABILITY TO ANTENNA THEORY

In the previous section, principles of compressed sensing for sparse signal recovery were introduced and recovery accuracy and probability were stated. An important question is now how to apply these methods to the antenna theory framework introduced in Chapter 2. The ultimate goal here is the significant reduction of sample points (and therefore sample time) required in near-field measurements of antennas. Current spherical scanners rotate around the AUT to capture samples on an equiangular grid. The density of measurement points is primarily determined by the electric size of the antenna. Scan times for large antennas at high frequencies are in the order of several hours to days. Consequently, scan time reduction via post processing of the gathered data appears to be very promising.

First, a short recap of Chapter 2 and Chapter 3 is provided for convenience. The field measured by a probe antenna with orientation

χ on a sphere with radius A and at angular position θ and ϕ can be developed into spherical modes as described by the transmission formula (cf. Equation 53)

$$w(A, \chi, \theta, \phi) = \sum_{\substack{smn \\ \mu}} Q_{smn} e^{im\phi} d^n_{\mu m}(\theta) e^{i\mu\chi} P_{s\mu n}(kA). \qquad (110)$$

In matrix notation this expansion can be written as (cf. Equation 59)

$$w = FQ \qquad (111)$$

and its inverse is formally written as

$$Q = F^{-1}w. \qquad (112)$$

If the measurement sphere around the antenna is sampled on an equiangular grid, very efficient techniques exist to solve Equation 112. These techniques take use of the special structure of the transmission formula and its similarity to the Fourier transform. In fact, solving the transmission formula for the coefficients Q only takes two discrete Fourier transforms over θ and ϕ and some additional processing [1]. This similarity is the reason why compressed sensing results which were originally developed for Fourier matrices are predestined for application in spherical wave expansions as well. In what follows it will be shown that the spherical sensing matrix F in fact satisfies the UUP and can therefore be used to reconstruct w by exploiting sparsity in Q.

4.2.1 *Uniform Uncertainty*

To be able to apply results from the compressed sensing framework, the respective quantities have to be identified. Table 5 provides an mapping of quantities from antenna theory to their counterparts in compressed sensing. The sampling domain is space with the samples at different locations specified by w. The sparsity domain is the spherical wave domain with the corresponding coefficients specified in Q. The transform linking spatial domain and spherical wave domain is defined by the matrix F.

The UUP condition in this new context now reads as

$$(1 - \delta_S)\|Q\|_2^2 \leqslant \|FQ\|_2^2 = \|w\|_2^2 \leqslant (1 + \delta_S)\|Q\|_2^2. \qquad (113)$$

To investigate for which isometry constants δ_S Equation 113 is satisfied, we first have to specify the sampling set Ω on which the measurements w are obtained.

Many commercially available spherical antenna scanners sample on a sphere surrounding the AUT on an equiangular grid. This allows for efficient calculation of the spherical coefficients Q [1] and

Table 5: Mapping of the quantities from compressed sensing to their counterparts in antenna theory.

	Compressed Sensing	**Antenna Theory**
sampled signal	$\hat{f}$	$\boldsymbol{w}$
supporting set	Ω	Ω
sparse signal	f	$\boldsymbol{Q}$
supporting set	T	T
sensing matrix	F_Ω	$\boldsymbol{F}$

will therefore be our starting point. Sampling on an equiangular grid means that the angular step Δ between two adjacent sampling points is constant for all sampling points,

$$(\boldsymbol{w})_l = w(A, \chi_l, \theta_l, \phi_l) \tag{114}$$

$$\theta_l = (l-1)\Delta \quad \mathrm{mod}\ \pi + \Delta \tag{115}$$

$$\phi_l = \left\lfloor \frac{l\Delta}{\pi + \Delta} \right\rfloor \Delta \quad \mathrm{mod}\ 2\pi + \Delta \tag{116}$$

$$\chi_l = \begin{cases} 0, & 1 \leqslant l \leqslant L/2 \\ \pi/2, & L/2 + 1 \leqslant l \leqslant L \end{cases} \tag{117}$$

with L being the total number of sampling points. L and Δ have to be chosen such that the whole sphere is reached for both probe orientation angles χ, i. e.

$$L = 2L_\theta L_\phi \tag{118}$$

$$\Delta = \frac{\pi}{L_\theta - 1} = \frac{2\pi}{L_\phi - 1}, \tag{119}$$

where L_θ and L_ϕ denote the number of different θ and ϕ values, respectively.

This complicated formulation of simple circumstances arises because the measurement data of a two-dimensional surface has to be organized somehow in a one-dimensional vector. Figure 13 provides a comprehensible depiction of this method for an angular step value $\Delta = \pi/4$. Figure 14 shows the same mapping on a three-dimensional sphere.

Now that the notion of an equiangular grid is established and the arrangement into the vector $\boldsymbol{w}$ is specified, the set of sampling locations Ω is defined to be a subset of the l-index set for equiangular sampling,

$$\Omega \subseteq \{1, 2, \dots, L\}. \tag{120}$$
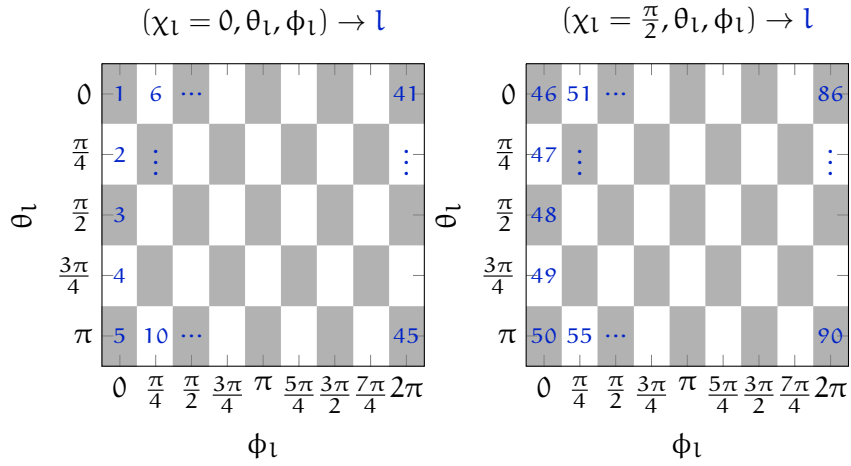
Figure 13: Definition of summation index l (blue) for an exemplary angular step size $\Delta = \frac{\pi}{4}$. The values of θ, ϕ and χ are numbered as depicted above. This allows for a two-dimensional data set to be arranged in an one-dimensional vector.
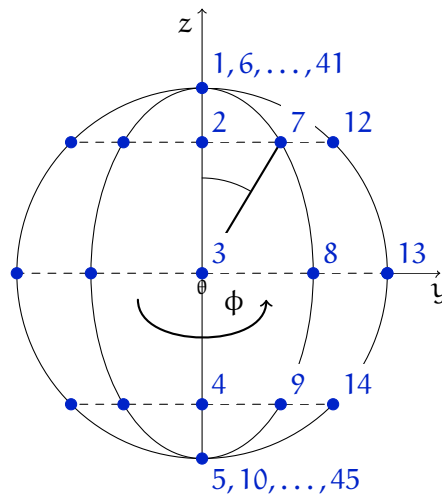
Figure 14: Three-dimensional depiction of the summation index l (blue) on the sphere for an exemplary angular step size $\Delta = \frac{\pi}{4}$ and $\chi_l = 0$. For $\chi_l = \pi/2$ the index l can be calculated by adding $L/2$, i.e. $l \rightarrow l + L/2$.

The quantity

$$\Omega_{(\chi,\theta,\phi)} = \{(\chi_l, \theta_l, \phi_l) : \quad l \in \Omega\} \tag{121}$$

specifies the set of orientation angles associated with the points in the sampling set Ω. Defining Ω as a subset of the l-index set is by no means necessary. It will, however, allow us to use efficient and numerically stable implementations of the spherical multipole transform.

As was already shown in Section 4.1, sensing matrices satisfy the UUP with high probability if the sampling set Ω is chosen at random. A uniform random distribution (as it is used for the Fourier matrix) will not take into account the underlying spherical geometry of our problem. That is why the UUP inequality

$$(1 - \delta_S)\|\mathbf{Q}\|_2^2 \leqslant \|\mathbf{w}\|_2^2 \leqslant (1 + \delta_S)\|\mathbf{Q}\|_2^2. \tag{122}$$

has to be considered again. The bounding factor $\|\mathbf{Q}\|_2^2$ is seen to accommodate for the total radiated power

$$P = \frac{1}{2} \sum_{smn} |Q_{smn}|^2 = \frac{1}{2} \sum_{j=1}^{J} |Q_j|^2 = \frac{1}{2}\|\mathbf{Q}\|_2^2 \tag{123}$$

of the measured source (cf. Equation 35). To achieve the smallest possible isometry constants δ_S, $\|\mathbf{w}\|_2^2$ has to approximate the transmit power as well as possible. Considering only tangential field components, the transmit power can be calculated by

$$
\begin{aligned}
P &= c_1 \int_0^{2\pi} \int_0^{\pi} \left(|E_\theta|^2 + |E_\phi|^2\right) \sin\theta \, d\theta \, d\phi \\
&\approx c_2 \sum_{l=1}^{L} |w(A, \chi_l, \theta_l, \phi_l)|^2 \sin\theta_l \Delta^2 \\
&= c_2 4\pi \sum_{l=1}^{L} |w(A, \chi_l, \theta_l, \phi_l)|^2 p\,(\theta_l)\, p\,(\phi_l) \\
&= c_2 4\pi E\left\{|w|^2\right\}
\end{aligned}
\tag{124}
$$

with sinusoidal probability density function

$$p\,(\theta_l) = \frac{\Delta \sin\theta_l}{2} \tag{125}$$

and the uniform probability density function

$$p\,(\phi_l) = \frac{\Delta \phi_l}{2\pi} \tag{126}$$

for angles from the equiangular sampling set. In the last line of Equation 124 the expected power of a sample regarding its spatial distribution is calculated. For $\|\mathbf{w}\|_2^2$ as close as possible to $\|\mathbf{Q}\|_2^2$, it is therefore beneficial to pick random samples according to the distributions in Equation 125 and Equation 126.

DEFINITION OF THE RANDOM SAMPLING SET Ω Following the considerations above, the random set of measurements Ω is created using the procedure below.

- Pick three realizations of a uniform random process.

$$U, V, W \sim \mathcal{U}(0, 1) \tag{127}$$

- Calculate spherical coordinates (θ, ϕ) which are distributed according to a uniform distribution on the unit sphere and calculate χ uniform in the interval $\chi \in [0, \pi/2]$.

$$\theta = \cos^{-1}(2U - 1) \tag{128}$$

$$\phi = 2\pi V \tag{129}$$

$$\chi = \frac{\pi}{2}W \tag{130}$$

- Find the closest neighbor in the complete set of equiangular sampling points $l \in 1, \ldots, L$.

$$l_\Omega = \arg\min_l \left\{ (\theta - \theta_l)^2 + (\phi - \phi_l)^2 + (\chi - \chi_l)^2 \right\} \tag{131}$$

- Add the index corresponding to the nearest set of spherical coordinates to the random sampling set.

$$\Omega = \Omega \cup \{l_\Omega\} \tag{132}$$

This procedure is repeated until the number of desired samples $|\Omega|$ is obtained. Figure 15 shows a comparison of the procedure above and a simple uniform distribution in the angular values. The proposed method (Figure 15a) guarantees uniform spacing between samples whereas the simple variant (Figure 15b) leads to a dense distribution of samples in the polar regions of the measurement sphere.

4.2.2 *Bounds for the Isometry Constant*

Now that the sampling set Ω is defined, the next step is to determine if the sensing matrix $\mathbf{F}$ satisfies the UUP with good isometry constants. In Section 4.1 it was shown that the UUP basically guarantees that a transform can never be localized (i. e. have small support) in both its original domain and its image domain. To analyze if the sensing matrix $\mathbf{F}$ satisfies this constraint, we will consider the worst possible case, namely the maximum directivity antenna. Supergain antennas, which under some circumstances have even higher directivity than maximum directivity antennas, are not considered here since they are highly inefficient and not relevant for the practical purposes considered in this thesis (cf. [19]).
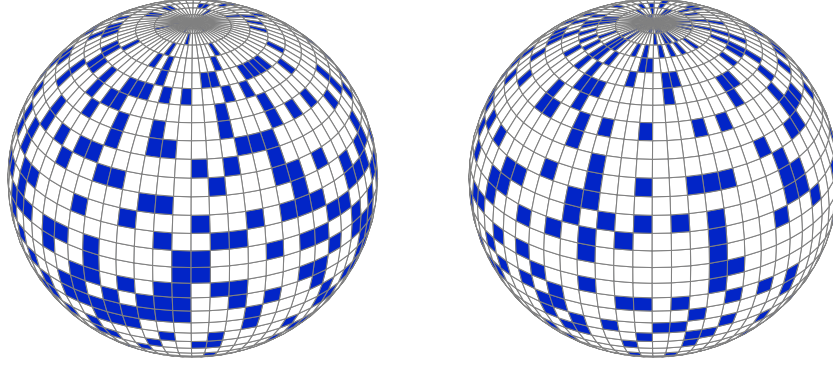
(a) Uniformly distributed sampling points on sphere.

(b) Dense distribution of sampling points in the polar regions.

Figure 15: Uniform sampling positions (left, blue) are distributed evenly over the sphere and are suitable for different antenna patterns. Uniform angular sampling in both θ and ϕ leads to a high density of sampling points in the polar regions (right, blue) and is therefore not desirable.

The maximum directivity antenna has the highest possible directivity for a given degree N_{MDA} [19],

$$D = N_{MDA}^2 + 2N_{MDA} \tag{133}$$

That means no other practical antenna allows stronger focusing of the electric field. The maximum number of coefficients necessary to characterize this antenna can be calculated using Equation 56 and amounts to

$$J = 2N_{MDA}(N_{MDA} + 2). \tag{134}$$

The sparsest possible representation of the maximum directivity antenna is achieved for maximum rotational symmetry of its field (the order m needed for representation of variations in ϕ is minimal in this case). The only non-zero coefficients $\mathbf{Q}$ for this orientation are given by [1] as

$$Q_{1,1,n} = Q_{2,1,n} = Q_{1,-1,n} = -Q_{2,-1} = -c\left(\frac{i^n}{2}\sqrt{2n+1}\right). \tag{135}$$

This specific constellation gives us the worst case for the UUP inequality and will therefore provide worst case bounds for the isometry constants δ_S. Every other antenna is either less localized in the coefficient domain or has a less focused electric field in the spatial domain. Figure 16a and Figure 16b show the normalized θ- and ϕ-components of a maximum directivity antenna and Figure 16c and Figure 16d show the corresponding multipole coefficients.
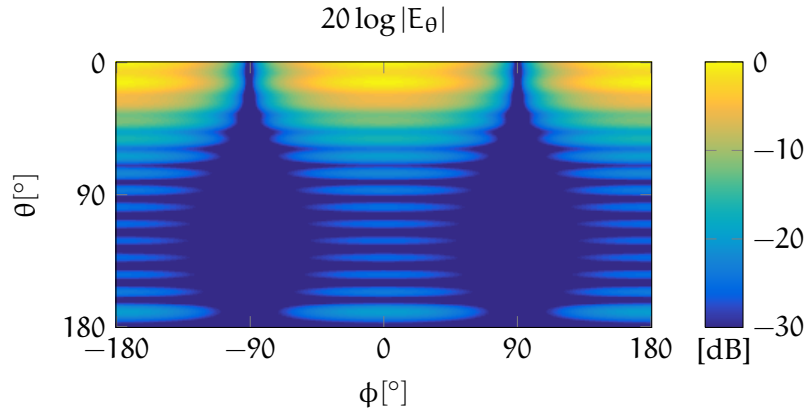
(a) Logarithmic depiction of E_θ of a maximum directivity antenna normalized to the maximum amplitude.
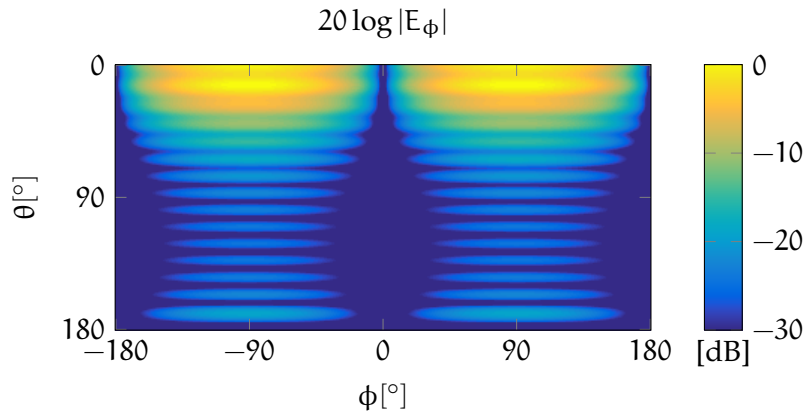
(b) Logarithmic depiction of E_ϕ of a maximum directivity antenna normalized to the maximum amplitude.
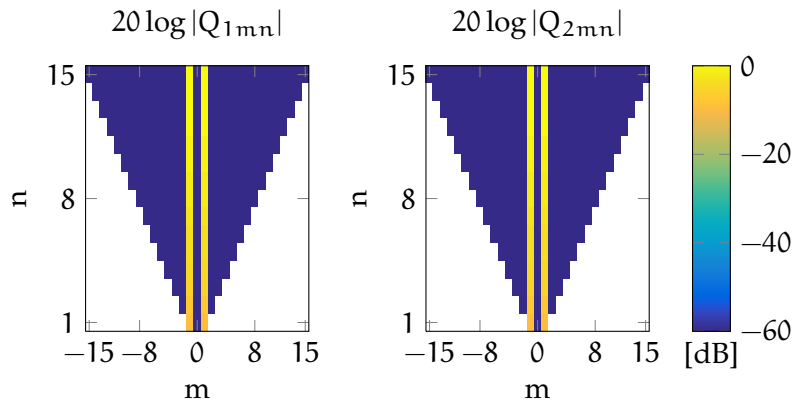
(c) Logarithmic depiction of $|Q_{1mn}|$ of a maximum directivity antenna normalized to the maximum value.

(d) Logarithmic depiction of $|Q_{2mn}|$ of a maximum directivity antenna normalized to the maximum value.

Figure 16: Field and coefficients of a maximum directivity antenna with degree $N_{MDA} = 15$.
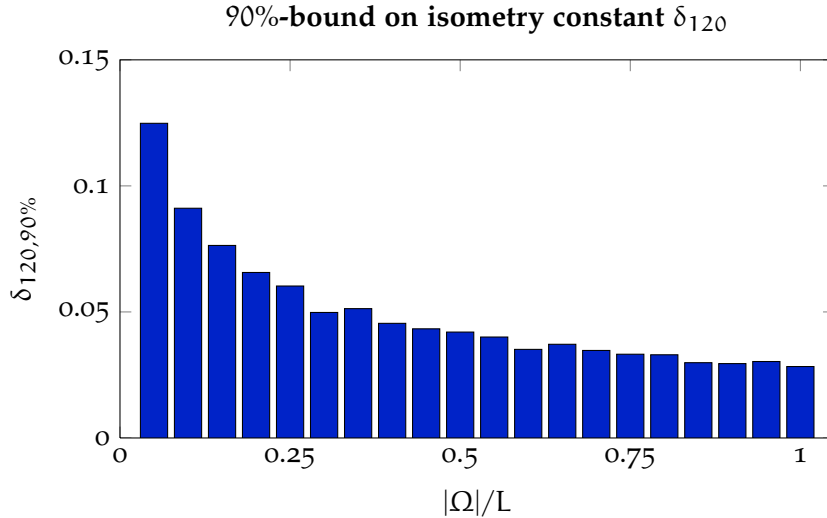
Figure 17: Bar plot of the upper bound on the isometry constant, $\delta_{120,90\%}$, over the support size Ω normalized to the size of the complete sampling set L. The probability of a realization of δ_{120} to be smaller than $\delta_{120,90\%}$ is 90%.

Since deriving analytical bounds for the isometry constants δ_S of a maximum directivity antenna is challenging and would exceed the scope of the thesis, a novel approach is suggested. The sampling set Ω is a random set and the isometry constants δ_S satisfying the UUP inequality are considered to be random as well. We will therefore analyze multiple realizations of the sampling set and its corresponding isometry constants and derive bounds for which a fixed percentage of realizations satisfies the UUP. Further, different sparsity levels $S = |T|$ are achieved by using maximum directivity antennas with different degree N_{MDA} while keeping the overall number of samples the same.

First, let us consider the case of a maximum directivity antenna with maximum degree $N_{MDA} = 30$. According to Equation 38, the cutoff degree $N = 40$ is chosen for the multipole expansion. The number of sampling points for the complete equiangular sampling set is $L = 2(2N + 1)(N + 1) = 6642$. The size of the supporting set for the spherical wave coefficients **Q** follows from Equation 135 to $S = |T| = 4N_{MDA} = 120$. Calculating 1000 realizations for the sampling set Ω and calculating the upper bound on the isometry constant which is larger than 90% of the δ_{120}-realizations leads to the results depicted in Figure 17. The UUP inequality is seen to be satisfied with very tight bounds δ_{120} in at least 90% of sampling set realizations.

When performing the same numerical evaluation for different support sizes (by using maximum directivity antennas with lower maximum degree and maintaining the number of equiangular samples L), an interesting issue arises (cf. Figure 18). Intuitively, the bound on the isometry constant is decreasing for decreasing support size S because fewer coefficients cause a less focused electric field. On the contrary,
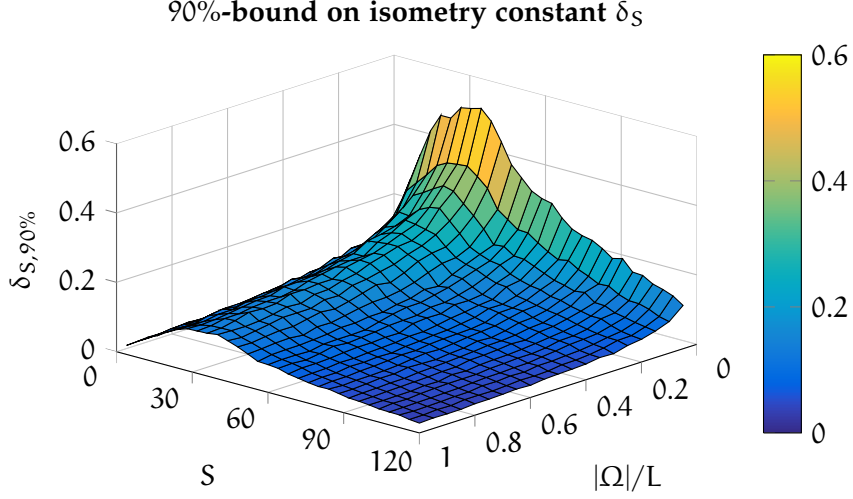
Figure 18: Depiction of the upper bound $\delta_{S,90\%}$ on the isometry constant δ_S for coefficient support size $S = |T|$ and sampling set support size $|\Omega|$. $S \approx 30$ constitutes the worst case scenario for which the upper bound is rather large.

fewer coefficients cause fewer sidelobes for the maximum directivity antenna, thus leading to less radiated power outside the main lobe. The worst case for which coefficient sparsity and low sidelobe level add up to large upper bounds on the isometry constant δ_S occurs for $N_{MDA} = 8 \ldots 10$.

Figure 19 shows the upper bound $\delta_{S,99\%}$ containing 99% of isometry constant realizations. Again, the largest bounds are found for $N_{MDA} = 8 \ldots 10$.

Considering now the condition in Equation 105 for the isometry constant, it is possible to search for the minimum number of sample points in Ω such that the program (P_1) recovers any sparse set of coefficients with support size S with given probability. The isometry bounds $\delta_{S,99\%}$, $\delta_{2S,99\%}$ and $\delta_{3S,99\%}$ are calculated for S in the range $S = 4, 8, \ldots, 40$ (corresponding to maximum directivity antennas with $N_{MDA} = 1, 2, \ldots 10$) and it is checked if the inequality

$$\delta_{S,99\%} + \delta_{2S,99\%} + \delta_{3S,99\%} \leqslant 1 \tag{136}$$

holds. The data obtained by the numerical evaluation described above suggests that Equation 136 holds for $S = 4, 8, \ldots, 40$ for all Ω satisfying

$$|\Omega| \geqslant 0.25L \tag{137}$$

with probability

$$P\{\delta_S + \delta_{2S} + \delta_{3S} \leqslant 1\} \geqslant 0.99^3 \approx 0.95 \,. \tag{138}$$

For noisy samples, the condition on the isometry constant

$$\delta_{3S} + 3\delta_{4S} \leqslant 2 \tag{139}$$
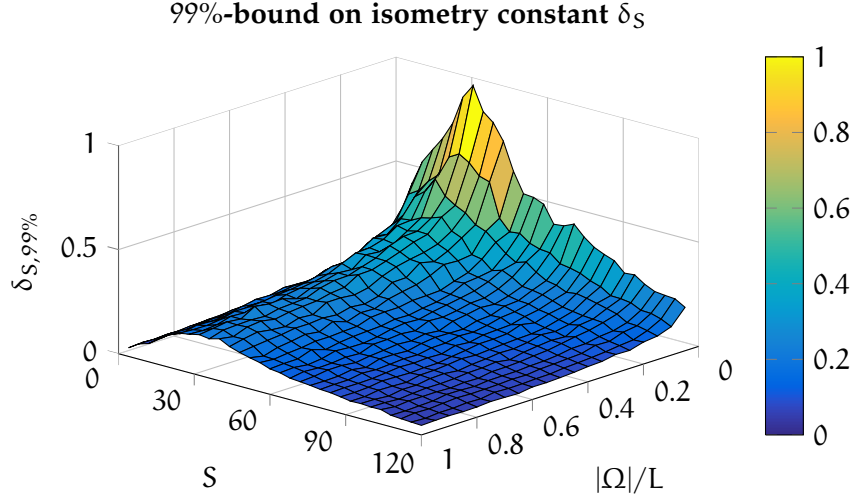
Figure 19: Depiction of the upper bound $\delta_{S,99\%}$ on the isometry constant δ_S for coefficient support size $S = |T|$ and sampling set support size $|\Omega|$. Again, $S \approx 30$ constitutes the worst case scenario for which the upper bound is rather large.

guarantees a bound on the error

$$\|\mathbf{Q}^{\sharp} - \mathbf{Q}\|_2 \leqslant C_S \|\mathbf{FQ} - w\|_2 \tag{140}$$

for the solution $\mathbf{Q}^{\sharp}$ of the reconstruction program (P_2) (cf. Equation 106 - Equation 108). The data obtained by the numerical evaluation described above suggests that Equation 139 holds for $S = 4, 8, \ldots, 40$ for all Ω satisfying

$$|\Omega| \geqslant 0.20L \tag{141}$$

with probability

$$P\{\delta_{3S} + 3\delta_{4S} \leqslant 2\} \geqslant 0.99^3 \approx 0.95. \tag{142}$$

The procedure used for deriving these approximate bounds is summarized in the following listing.

- The field of a maximum directivity antenna is calculated on L equiangular grid points.

- For a given realization of the random sampling set Ω, the corresponding realization of the isometry constant (cf. Equation 122) is calculated.

- The above step is repeated 1000 times and an upper bound $\delta_{S,99\%}$ is calculated which is larger than 99% of the isometry constant realizations.

- The upper steps are repeated for different support sizes S.

- The size of the random sampling set $|\Omega|$ for which Equation 136 holds is determined.

- The data gathered by the steps above suggest that only 25% of the sampling points from the complete equiangular sampling set are needed to recover the field of an arbitrary antenna with support size $S \leqslant 40$ by using the program (P_1) with probability larger than 95%.

- Further, the experiment suggests that only 20% of the sampling points from the complete equiangular sampling set are needed to recover the field of an arbitrary antenna with support size $S \leqslant 40$ by using the program (P_2) with probability larger than 95% and error constraint.

This is a remarkable result since it suggests that we only have to measure one quarter of the sampling points previously needed to characterize an antenna (under the condition of sparse wave coefficients). An adequate spatial sampling pattern can therefore save up to 75% of measurement time because fewer samples have to be obtained. In the next chapter, we will support these theoretical results with simulation data.

The cutoff degree $N = 40$ which was used for the numerical estimation of the bound on $|\Omega|$ was chosen arbitrarily. However, choosing a larger cutoff degree and simulating larger maximum directivity antennas (i.e. larger N_{MDA}) will lead to increased sidelobe radiation and will decrease the bounds on the isometry constant. Lower cutoff degrees are not considered here because they are not part of the use case. For low cutoff degrees, sampling time is low and a method for sampling time reduction can therefore not gain much and is not worth the effort.

4.3 TRUNCATION HANDLING

Often measurement issues arise due to the mechanical structure of spherical antenna scanners limiting the accessibility of parts of the measurement sphere. Typically, this fact leads to a truncation of the measurement sphere for angles larger than a certain threshold. Much scientific work concentrated on different approaches to solve this issue. In [20] an LS-estimation method with energy constraint is deployed whereas [21] suggests an iterative approach using the band-limitation for antennas. In [22] an iterative approach is compared to an equivalent current method with subsequent extrapolation.

The compressed sensing framework which was developed in the previous chapter allows for a very different approach to this problem. The truncated measurement sphere can be seen as a random set of sampling positions Ω containing all measurement points on the

equiangular grid which are accessible by the scanner, see Figure 20. Solving the program (P_1) in a very similar manner as in the previous section, we can find a coefficient set $\mathbf{Q}$ which on the one hand explains the observations $\mathbf{w}$ and on the other hand is sparse. This approach has the favorable feature that it does not introduce additional complexity in the coefficients. It searches for the simplest solution which still explains the measurements. This is not guaranteed for the other methods mentioned above. A deeper investigation of the proposed truncation handling method is unfortunately out of the scope of this thesis. However, further research in this area seems very promising.
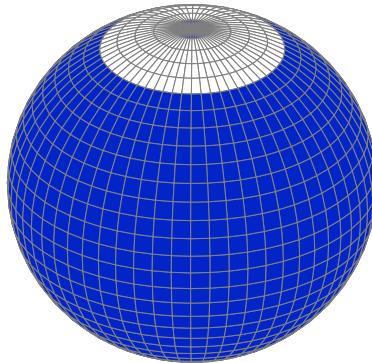
Figure 20: Sampling scheme on the sphere for truncation handling, i. e. if a small area (white) cannot be sampled due to mechanical limitations.

RECONSTRUCTION EVALUATION

Due to the popularity of compressed sensing in the resent years, the research area of minimization methods attracted a lot of attention as well. There is a huge number of adequate solvers available for the so called *basis pursuit*

$$(P_1) \qquad \min_{g} \|g\|_1 \quad \text{s.t.} \quad \hat{g}(k) = \hat{f}(k), \, k \in \Omega \qquad (143)$$

and the so called *basis pursuit de-noising*

$$(P_2) \qquad \min_{g} \|g\|_1 \quad \text{s.t.} \quad \|F_\Omega g - \hat{f}\|_2 \leqslant \epsilon \qquad (144)$$

which are the recovery algorithms introduced in the previous chapter. The choice of the right solver is primarily determined by the size of the problem. For small-scale and medium-scale applications, classical convex optimization methods (e.g. [23]) can be applied. For large-scale problems, where the number of unknowns is in the thousands or millions, iterative thresholding and message passing techniques are often employed [24].

Since antenna measurements at high frequencies require thousands of sampling points, a large-scale solver is necessary to reconstruct our measurement. The interior point method described in [25] will be used in what follows to solve Equation 143 and Equation 144. It is specifically suitable for our purposes because there exists a readily available Matlab implementation (cf. [26]) which does not require explicit knowledge of the sensing matrix F. Instead, a function handle can be supplied to take full advantage of an efficient, FFT-based Matlab implementation for the transform $w = FQ$.

The choice of the specified solver is by no means mandatory. Equal or even better results are achievable with a variety of other methods. However, searching for the optimal solver is out of the scope of this thesis.

The remaining chapter addresses the question of solving the reconstruction problem with a reduced number of sampling points. After the basic concepts of the selected solver are introduced, synthetic as well as measurement data is reconstructed. For antennas with non-sparse coefficient set, an iterative algorithm is introduced which allows for successful reconstruction in a large variety of scenarios.

We will focus on the basis pursuit de-noising problem given in Equation 144 because it incorporates measurement noise. With the samples w measured on the random set Ω, the sensing matrix $\mathbf{F}$ and the (hopefully) sparse multipole coefficients $\mathbf{Q}$, our problem reads as

$$\min_{\mathbf{Q}} \|\mathbf{Q}\|_1 \quad \text{s.t.} \quad \|\mathbf{FQ} - w\|_2 \leqslant \epsilon. \tag{145}$$

In what follows, the reconstruction problem is recast so that the interior point solver of [25] can be applied. This method is shortly summarized in the following.

The reconstruction problem of Equation 145 can be equivalently described as an unbounded optimization problem

$$\min_{\mathbf{Q}} \|\mathbf{FQ} - w\|_2^2 + \lambda \|\mathbf{Q}\|_1 \tag{146}$$

or as a quadratic problem with linear inequality constraints

$$\begin{aligned} \min_{\mathbf{Q}} \quad & \|\mathbf{FQ} - w\|_2^2 + \lambda \sum_{j=1}^{J} u_j \\ \text{s.t.} \quad & -u_j \leqslant Q_j \leqslant u_j, \quad j = 1, \dots, J. \end{aligned} \tag{147}$$

The box constraints $-u_j \leqslant Q_j \leqslant u_j$ are now accounted for by introducing the logarithmic barrier

$$\Phi(\mathbf{Q}, u) = -\sum_{j=1}^{J} \log\left(u_j + Q_j\right) - \sum_{j=1}^{J} \log\left(u_j - Q_j\right) \tag{148}$$

what allows to define the central path as the unique minimizer $(\mathbf{Q}^*(t), u^*(t))$ of the convex function

$$\Phi_t(\mathbf{Q}, u) = t \min_{\mathbf{Q}} \|\mathbf{FQ} - w\|_2^2 + t \sum_{j=1}^{J} \lambda u_j + \Phi(\mathbf{Q}, u) \tag{149}$$

with the parameter $t \in (0, \infty)$ specifying the steepness of the logarithmic barriers. Starting on a central point $(\mathbf{Q}^*(t_0), u^*(t_0))$, the next point on the central path $(\mathbf{Q}^*(t_1), u^*(t_1))$ is calculated for an increased value $t_1 > t_0$. Usually, Newton's method is used to minimize Equation 149. But considering the size of the problem, inversion of the Hessian is prohibitively complex. That is why the inverse Hessian is approximated using a preconditioned conjugate gradient approach. After the minimization using the approximate inverse Hessian, the logarithmic barrier factor t is increased and a new central point is calculated. If the inverse Hessian can be approximated accurately enough, this procedure leads to an optimal solution for Equation 147. For additional details and derivations concerning the above

Table 6: Input parameters of the Matlab function `l1_ls` and the respective quantities in antenna theory.

l1_ls input	Notation	Explanation
A	$\mathbf{F}$	Sensing matrix
At	$\mathbf{F}^{-1}$	Transposed sensing matrix
m	$|\Omega|$	Number of observations
n	J	Number of unknowns
y	$\boldsymbol{w}$	Measurement samples
lambda	λ	Regularization parameter
rel_tol	$\epsilon/\|\mathbf{Q}\|_2^2$	Relative accuracy
quiet	*default*	Controls displayed information
x0	*default*	Starting vector
u0	*default*	Starting bounds
t0	t_0	Starting boundary weight

summary, the reader is referred to the original literature in [25]. Additionally, [27] provides a broad overview on convex optimization.

The Matlab implementation `l1_ls` [26] of the method above allows to specify the quantities listed in Table 6.

Choosing the right parameters λ and t_0 is no easy task. The regularization parameter $\lambda > 0$ influences the sparsity of the optimal coefficient set $\mathbf{Q}^*$ (cf. Equation 146). For large values of λ, the 1-norm has more weight in the minimization and the solution will have few non-zero entries. For small regularization parameters, the solution to Equation 146 will degrade to a LS-fit with many non-zero entries. Finding a balanced value for λ is therefore crucial.

The starting boundary weight t_0 determines if the "strictness" of the logarithmic barriers. For $t_0 \to 0$ the only term contributing to the function being minimized in Equation 149 is the logarithmic barrier. For $t_0 \to \infty$, the minimization problem degrades to an unbounded problem since the logarithmic barriers do not contribute to the function being minimized. A correctly chosen value for t_0 ensures fast convergence while maintaining all constraints.

5.1.1 *Solver Parameters*

We will now run a small numerical experiment to find suitable values for the regularization parameter λ and the starting boundary weight t_0. For this, a fixed value of t_0 is chosen and λ is iterated over a large span of possible values with logarithmic spacing. For the reconstruction, a maximum directivity antenna with $N_{\mathrm{MDA}} = 30$ and cutoff degree $N = 40$ is chosen. Following the insights of Chapter 4, 25% of the sampling points of the complete equiangular sampling grid are

Reconstruction error for multiple boundary weights
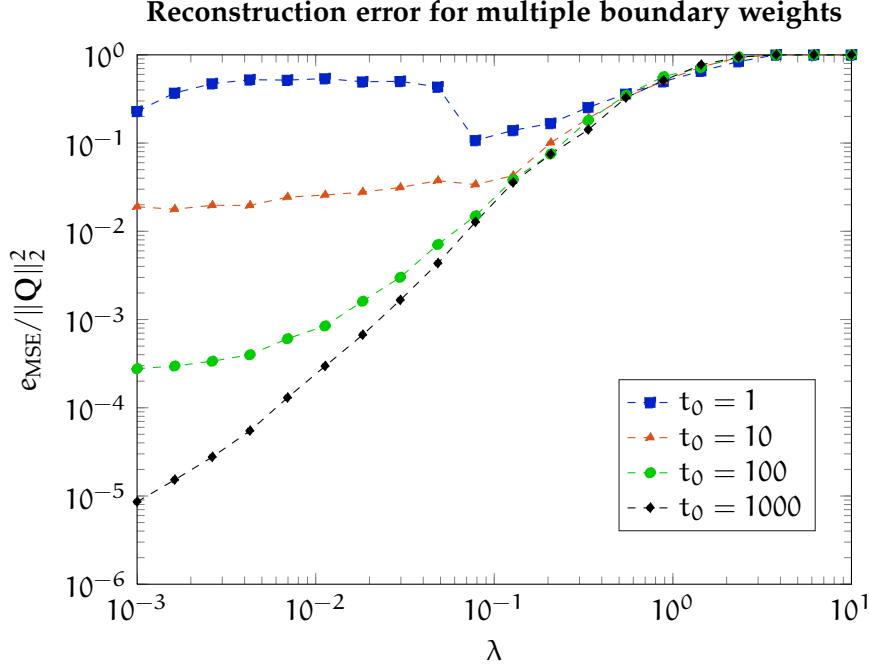
Figure 21: MSE of the reconstructed multipole coefficients for a maximum directivity antenna. Small values of λ and large t_0 are the favorable parameter setting.

taken into account. The performance metric will be the Mean Square Error (MSE) of the reconstructed multipole coefficients $\mathbf{Q}^\sharp$ to the original coefficients $\mathbf{Q}$, i.e.

$$e_{\mathrm{MSE}} = \frac{1}{M} \sum_{i=1}^{M} \|\mathbf{Q}^\sharp - \mathbf{Q}\|_2^2, \tag{150}$$

with the number of runs $M = 10$ for one value of λ.

Figure 21 shows the resulting MSE for $\lambda \in [10^{-3}, 10^1]$ and for $t_0 \in \{1, 10, 100, 1000\}$. For small values of t_0, the logarithmic barriers are dominant and corrupt the minimization. For $t_0 \geqslant 10$, the MSE decreases and the reconstruction successfully converges. For $\lambda \approx 1$ the 1-norm in Equation 146 is dominant and the minimum solution for the multipole coefficients is therefore the trivial all-zero solution. Regularization parameters which ensure good reconstruction properties are located in the interval $[10^{-3}, 10^{-2}]$. It is noted that for $\lambda \ll 10^{-3}$, the minimization degrades into a LS-problem. From now on, unless stated otherwise, we will choose a regularization parameter λ of 10^{-3} and an initial boundary weighting factor $t_0 = 1000$.

5.1.2 *Maximum Directivity Antenna*

With the solver parameters found in the previous chapter, we can now investigate the reconstruction of the field of a maximum directivity antenna in detail. As it is explained in Chapter 4, this specific

antenna type poses a worst case scenario for the reconstruction because of its highly localized field. Again, the field of a the AUT is randomly sampled on the measurement sphere. The number of samples is chosen to be 25% of the number of samples in the complete equiangular sampling set which is usually necessary to characterize this antenna.

Figure 22a shows the original tangential field of a maximum directivity antenna with $N_{MDA} = 30$. For an antenna like this, the complete equiangular sampling grid consists of $L = 2(2N+1)(N+1) = 6642$ sampling points [1] with the cutoff degree $N = 40$ chosen according to Equation 38. When choosing $0.25L \approx 1660$ samples randomly from the complete equiangular sampling grid and carrying out the minimization of Equation 146 with the parameters found in the previous section, we achieve the reconstructed fields $w^\sharp$ depicted in Figure 22b. The reconstruction error depicted in Figure 22c is seen to be insignificant.

5.2 ITERATIVE RECONSTRUCTION

Until now, only synthetic measurement data which is sparse by design and noiseless was considered. To be able to apply reconstruction algorithms to real world measurements of arbitrary antennas, a novel scheme is introduced. Broadly speaking, this scheme reconstructs the multipole coefficients of a given antenna in the coordinate system where those coefficients are sparsest. For this, the insights of Chapter 3 and Chapter 4 are condensed into an iterative reconstruction algorithm which is outlined in the following.

RECONSTRUCTION First, Equation 146 is carried out to find a set of coefficients $Q^{(k)}$ which at this point is not necessarily sparse. Usually, the field $w^{(k)} = F^{-1}Q^{(k)}$ associated with this set of coefficients is just some sort of interpolation of the random samples w.

PHASE CENTER As a next step, the newly found multipole coefficients $Q^{(k)}$ are translated into the phase center of the antenna, following Equation 80. This step yields a new coefficient set $Q_{shift}^{(k)}$ which is by definition sparser than before.

ROTATIONAL SYMMETRY Now a similar step is carrier out, only that the translation is replaced by a rotation. Following Equation 89, the translated coefficients are now rotated. As before, this step yields a new coefficient set $Q_{rotate}^{(k)}$ which is by definition sparser than before.

ITERATE With the newly found sparse coefficient set, a better reconstruction according to Equation 109 of the multipole coefficients

$20 \log |w(0, \theta, \phi)|$ $20 \log |w(\pi/2, \theta, \phi)|$
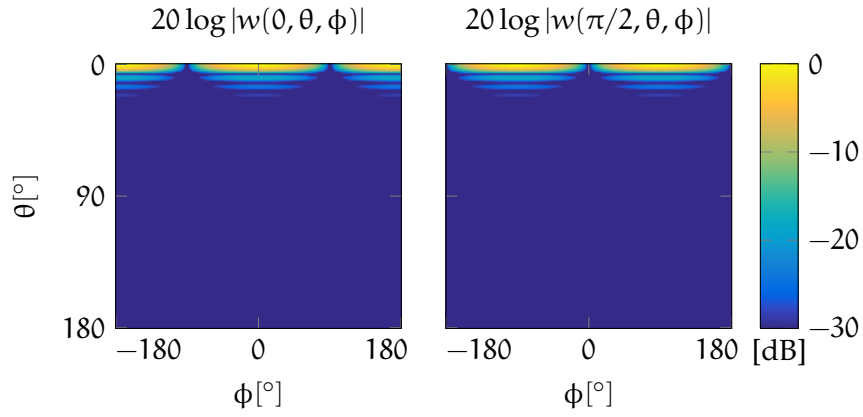
(a) Logarithmic depiction of the tangential field of a maximum directivity antenna normalized to the maximum amplitude.

$20 \log |w^\sharp(0, \theta, \phi)|$ $20 \log |w^\sharp(\pi/2, \theta, \phi)|$
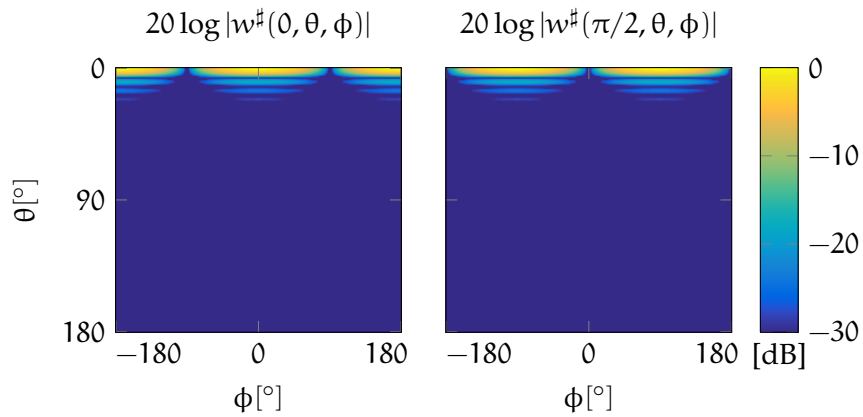
(b) Logarithmic depiction of the reconstructed tangential field of a maximum directivity antenna normalized to the maximum amplitude. Only 25% of the complete equiangular grid points are used in the reconstruction.

$20 \log |w^\sharp(0, \theta, \phi) - w(0, \theta, \phi)|$ $20 \log |w^\sharp(\pi/2, \theta, \phi) - w(\pi/2, \theta, \phi)|$
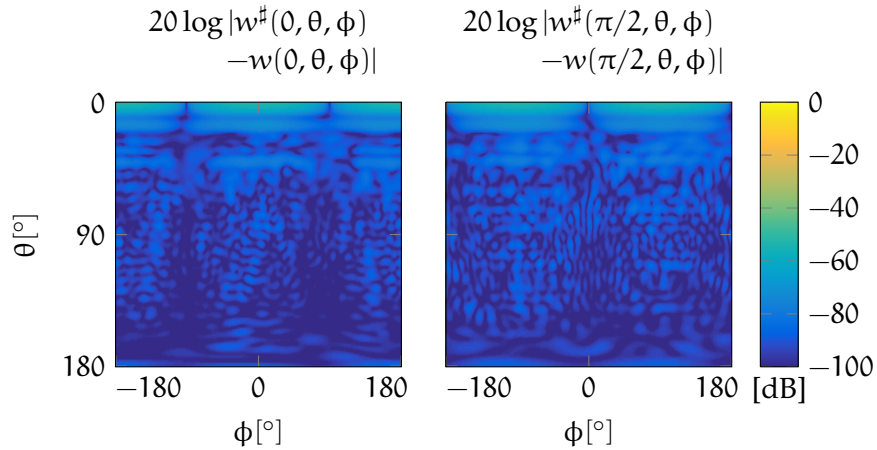
(c) Logarithmic depiction of the reconstruction error which stays below -50dB on the whole sphere.

Figure 22: Original (first row) and reconstructed (second row) tangential field of a maximum directivity antenna with $N_{\text{MDA}} = 30$ normalized to the maximum absolute value. The reconstruction error $|w^\sharp - w|$ is insignificant on the whole measurement sphere.

is possible, yielding $\mathbf{Q}^{(k+1)}$. This in turn leads to improved estimations of the phase center and rotational symmetry. The iteration can be stopped when the difference $\|\mathbf{Q}^{(k+1)} - \mathbf{Q}^{(k)}\|_2$ becomes small.

In mathematical terms, this algorithm reads as follows.

1. Take $|\Omega|$ random samples w uniformly spaced on the sphere.

2. Perform reconstruction

$$\mathbf{Q}^{(k)} = \arg\min_{\mathbf{Q}} \|\mathbf{Q}\|_1 \quad \text{s.t.} \quad \|\mathbf{FQ} - w\|_2 \leqslant \epsilon \tag{151}$$

3. Translate into estimated phase center

$$\mathbf{Q}^{(k)}_{\text{shift}} = \mathbf{T}^{(k)} \mathbf{Q}^{(k)} \tag{152}$$

4. Rotate to achieve rotational symmetry

$$\mathbf{Q}^{(k)}_{\text{rotate}} = \mathbf{R}^{(k)} \mathbf{Q}^{(k)}_{\text{shift}} = \mathbf{R}^{(k)} \mathbf{T}^{(k)} \mathbf{Q}^{(k)} \tag{153}$$

5. Perform reconstruction

$$\begin{aligned} \mathbf{Q}^{(k+1)} &= \arg\min_{\mathbf{Q}} \|\mathbf{Q}\|_1 \\ &\text{s.t.} \quad \|\mathbf{FT}^{-1,(k)} \mathbf{R}^{-1,(k)} \mathbf{Q} - w\|_2 \leqslant \epsilon \end{aligned} \tag{154}$$

6. Repeat steps $3-5$ for $k \to k+1$ until

$$\|\mathbf{Q}^{(k+1)} - \mathbf{Q}^{(k)}\|_2 < \epsilon_{\text{stop}} \tag{155}$$

Following this procedure, a sparse set of coefficients representing the AUT can be found as well as the translation and rotation matrices to obtain the (not necessarily sparse) coefficients in the original coordinate system.

5.2.1 *Horn Antenna*

To establish the proposed method, a horn antenna at 2.6GHz is considered. Measurements of this antenna are taken in the anechoic chamber at the Institute of Telecommunication of TU Wien. The measurements are obtained with a spherical scanner covering the azimuth angles $\phi \in [0°, 360°]$ and the polar angles $\theta \in [0°, 160°]$. To recover the missing samples for $\theta \in [160°, 180°]$ which are blocked by the supporting structure, an iterative estimation as described in [21] is used. Since the horn antenna is mounted with a small offset to the coordinate origin, we expect the multipole coefficients to be non-sparse. Moreover, noise is present in the measurement samples.

The MRE of the antenna (which is the radius of the smallest sphere centered at the origin and fully enclosing the AUT) is 0.8m, the cutoff degree therefore amounts to $N = 54$. The number of samples necessary to calculate the multipole coefficients with the standard FFT-based algorithm from [1] is $L = 2(2N + 1)(N + 1) = 11990$. We will try to reconstruct the coefficients with as little as $0.25L \approx 2997$ samples using the iterative reconstruction algorithm described above. Again, the regularization parameter $\lambda = 10^{-3}$ is chosen. Since the obtained measurement data is normalized at some point in the preprocessing at the measurement chamber, the starting boundary weight has to be changed and is chosen to be $t_0 = 1$.

Figure 23 shows the resulting reconstructed field of the iteration method. The first iteration (first row) shows large deviations from the original field (fourth row) which is calculated using the complete equiangular sampling grid. The translation to the estimated phase center and the rotation to achieve rotational symmetry in the first iteration provide a coefficient set which is sparse so that already the second iteration (second row) constitutes a good approximation of the actual field. A subsequent iteration step refines this approximation (third row).

Figure 24 shows the difference of the reconstructed field to the reference field for three iterations. While the reconstruction error is quite large after the first iteration (first row), the error decreases with every iteration. After the third step (third row), the error is below -17dB for all polar angles $\theta < 150°$. For polar angles $\theta > 150°$, we see larger deviations from the reference field. This effect arises due to the different approaches concerning truncation handling. The reference field is calculated using an iterative approach to recover the samples which cannot be measured in the test chamber. The iterative approach recovers those samples in a way that minimizes $\|\mathbf{Q}\|_1$. The difference of these two approaches causes the differences in the region $\theta > 150°$. A further discussion of this fact can be found in Section 4.3.

Table 7 lists the relative reconstruction error for three iterations. The error is seen to decrease with every iteration due to the optimization of the reconstruction coordinate system and the resulting sparsity of the multipole coefficients. A residual error remains since the truncation of the scan area introduces artifacts which cannot be compensated with the current approach.

Concluding this chapter, it is stated that we were able to recover both synthetic and real world measurements with a highly reduced sampling set using principles from the compressed sensing framework. For both synthetic and real world measurement, 25% of the sampling points usually needed for efficient FFT-based analysis is sufficient to recover the field of an antenna with good accuracy. This
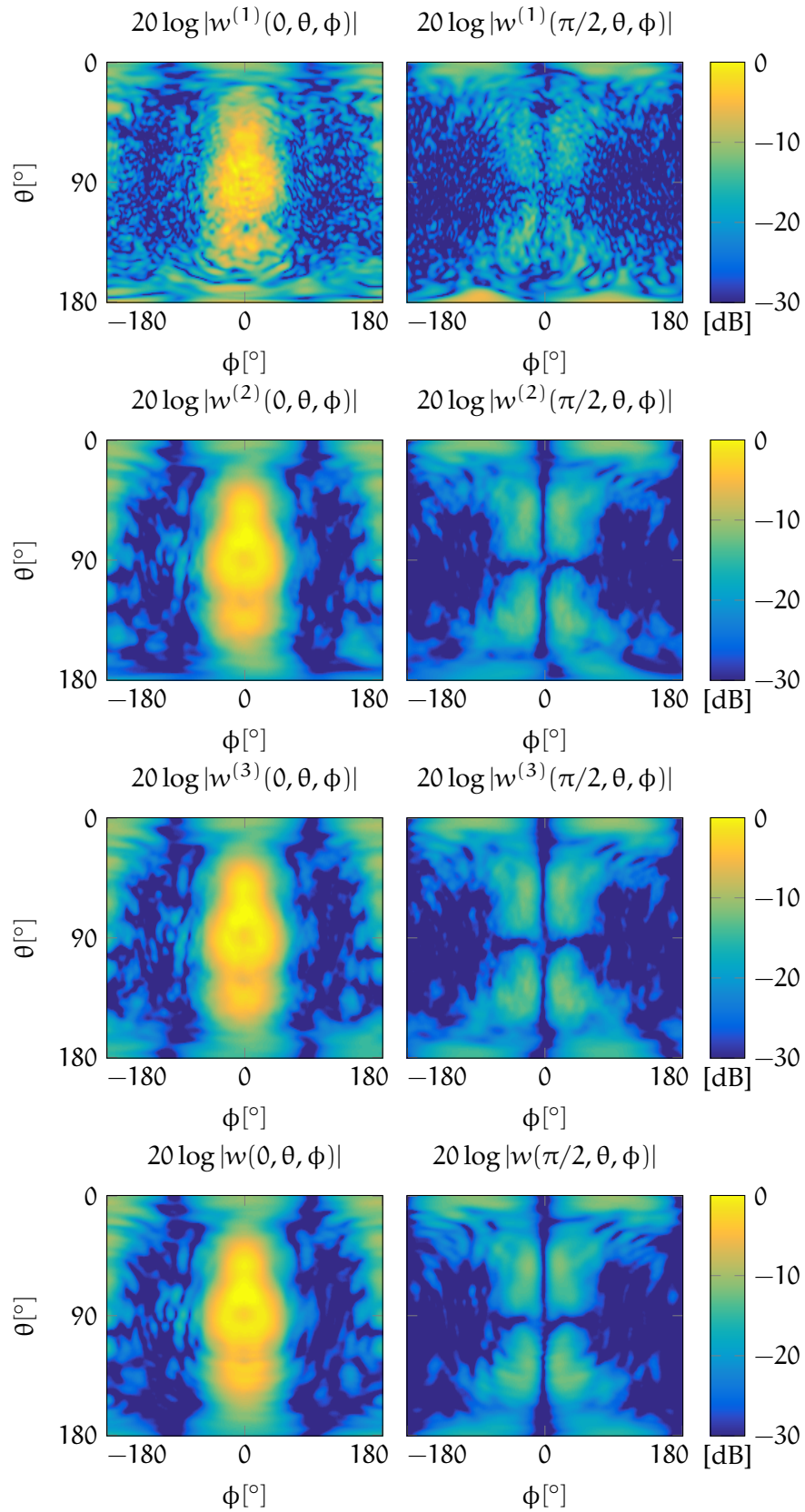
Figure 23: Depiction of the normalized reconstructed tangential field for three iterations (rows 1-3) and the actual field (row 4), respectively.
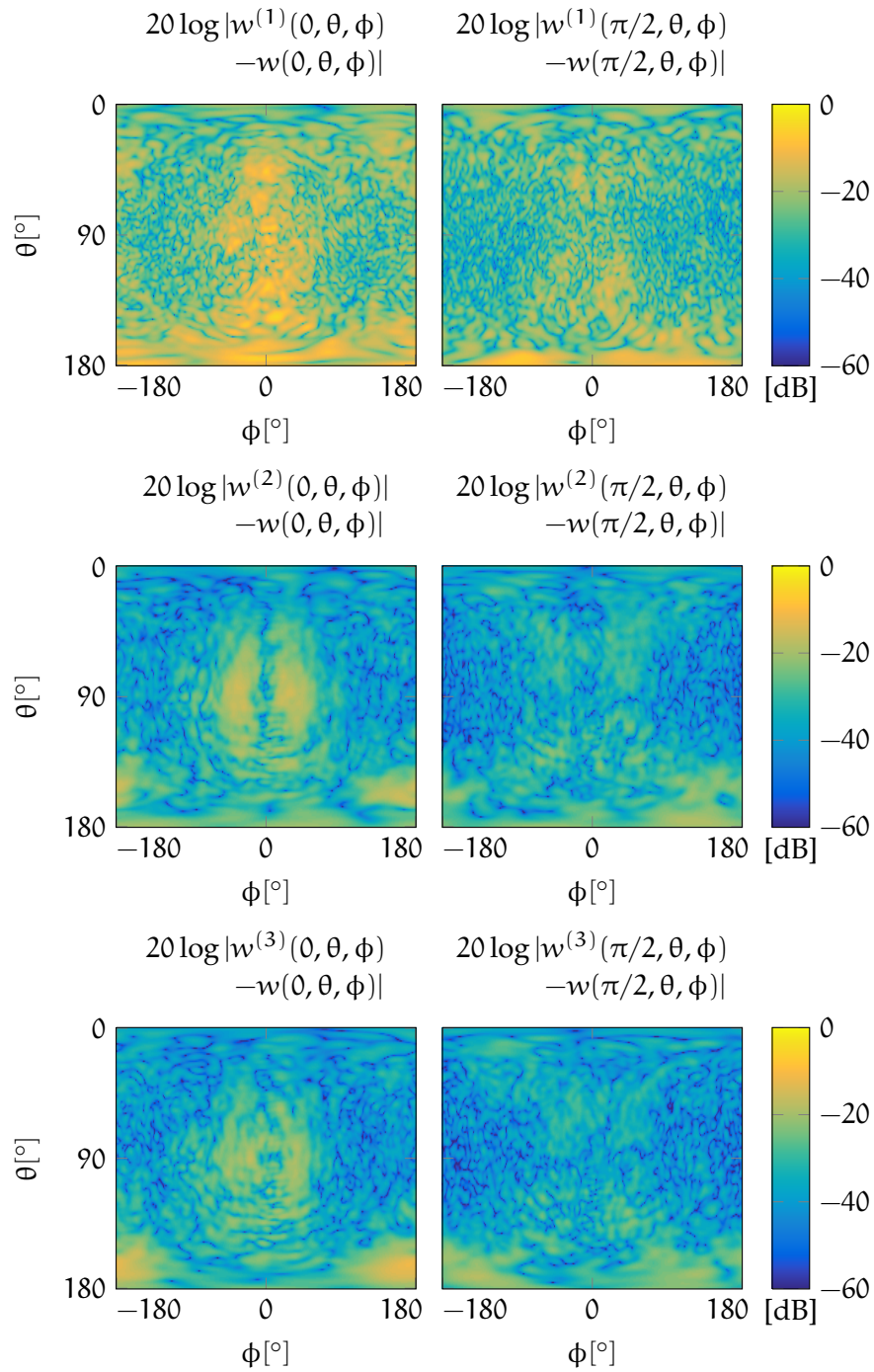
Figure 24: Depiction of the reconstruction error for three iterations (rows 1-3, respectively). Each iteration reconstructs the original field better then the one before due to the optimized coordinate transformation. The errors for $\theta \in [160°, 180°]$ are caused by the truncation of the scan area and the different estimation methods for this area.

Table 7: Reconstruction error relative to the total transmitted power for three iterations. The residual error after three iterations is mostly due to the different truncation handling techniques.

Iteration	$\|\mathbf{Q}^{(k)} - \mathbf{Q}\|_2 / \|\mathbf{Q}\|_2$
$k = 1$	0.392
$k = 2$	0.153
$k = 3$	0.129

results in the potential of significantly reducing measurement time in antenna characterization since fewer samples have to be acquired.

CONCLUSION

This thesis addresses the issue of measurement time reduction in spherical near-field measurements by reducing the number of sampling points necessary to characterize a radiating source. Since measurements of large antennas at high frequencies often take several hours, cutting on measurement time increases the efficiency of antenna characterization facilities. To achieve this goal, principles of compressed sensing are applied to determine the radiated fields without knowledge of the complete sampling grid. This thesis demonstrates the potential of reducing the number of necessary samples for FFT-based antenna characterization by as much as 75%, leading to a significant reduction in measurement time when implemented appropriately.

Chapter 2 and Chapter 3 provide the mathematical framework for finding the sparsity transform, i. e. the spherical multipole expansion, and for optimizing the coordinate system (by translation and rotation operations) so that the coefficient set of a given antenna is sparse. Moreover, a newly developed phase center estimation method is compared to a well known LS-based approach and, while being computationally more expensive, proves to increase mean accuracy by a factor of 200.

The concept of compressed sensing and its applicability to antenna theory is discussed in Chapter 4. In this context, it is shown that the posed problem satisfies the UUP condition with high probability given an appropriate sampling pattern on the sphere, thus allowing for reconstruction of the field in spite of undersampling. An empirical value of 25% of the complete equiangular sampling grid is given which still offers good reconstruction properties.

In Chapter 5 it is shown that an antenna can be characterized with as little as 25% of measurement points which are normally used in antenna characterization, given that the antenna's multipole coefficients are sufficiently sparse. If this is not the case, an iterative scheme is introduced which solves the reconstruction problem in an optimized coordinate system which renders the coefficients sparse again.

FURTHER WORK   Due to the limited scope of this thesis, some aspects were not treated with the thoroughness they deserve, thus providing foundation and inspiration for future research. The most notable considerations are listed below.

- The UUP condition is only analyzed with a numerical experiment considering the worst case scenario of a maximum direc-

tivity antenna. The close similarity of the multipole expansion and the two-dimensional Fourier transform suggests that analytical results which exist for the Fourier transform can be transfered to the multipole expansion. This would lead to a closed form stating the number of samples necessary to fulfill the UUP with high probability for a given level of sparsity.

- The choice of the reduced sampling set as a random subset of the complete equiangular sampling set is reasonable but arbitrary. Other choices for the reduced sampling set can lead to improved reconstruction properties while facilitating the actual sampling progress. Star- or spriral-shaped sampling trajectories have already proved their usefulness in similar measurement setups.

- As already indicated in the previous chapters, the proposed iterative algorithm can be used to reconstruct truncated scan areas. The investigation of this method's performance compared to methods already in use seems to be a promising research area.

- The choice of the solver used for the minimizing problem was again reasonable but arbitrary. Optimizing the solver for the minimization problem (e. g. by choosing a different preconditioner in the inverse Hessian approximation) leads to better convergence properties and possibly to better results. Moreover, the solver parameters have a huge influence on the reconstruction quality and are therefore suited for further investigation.

[1] J. E. Hansen, ed., *Spherical Near-field Antenna Measurements*. Institution of Engineering and Technology, 1988.

[2] T. B. Hansen, "Complex-point dipole formulation of probe-corrected cylindrical and spherical near-field scanning of electromagnetic fields," *IEEE Transactions on Antennas and Propagation*, vol. 57, no. 3, pp. 728–741, 2009.

[3] T. Laitinen and O. Breinbjerg, "A first/third-order probe correction technique for spherical near-field antenna measurements using three probe orientations," *IEEE Transactions on Antennas and Propagation*, vol. 56, no. 5, pp. 1259–1268, 2008.

[4] C. H. Schmidt, M. M. Leibfritz, and T. F. Eibert, "Fully probe-corrected near-field far-field transformation employing plane wave expansion and diagonal translation operators," *IEEE Transactions on Antennas and Propagation*, vol. 56, no. 3, pp. 737–746, 2008.

[5] P. N. Betjes, "An algorithm for automated phase center determination and its implementation," in *29th Annual Symposium of the Antenna Measurement Techniques Association*, (St. Louis, MO, USA), pp. 190–195, 2007.

[6] W. Kunysz, "Antenna phase center effects and measurements in GNSS ranging applications," in *14th International Symposium on Antenna Technology and Applied Electromagnetics & the American Electromagnetics Conference*, (Fairmont Chateau Laurier Ottawa, ON, Canada), pp. 181–184, 2010.

[7] P. Padilla de la Torre, J.-M. Fernandez Gonzalez, J. L. Padilla, G. Exposito-Dominguez, M. Sierra-Castaner, and B. Galocha Iraguen, "Comparison of different methods for the experimental antenna phase center determination using a planar acquisition system," *Progress In Electromagnetics Research*, vol. 135, pp. 331–346, 2013.

[8] J. Fridén and G. Kristensson, "Calculation of antenna radiation center using angular momentum," *IEEE Transactions on Antennas and Propagation*, vol. 61, no. 12, pp. 5923–5930, 2013.

[9] E. J. Candès, J. Romberg, and T. Tao, "Robust uncertainty principles: Exact signal reconstruction from highly incomplete frequency information," *IEEE Transactions on Information Theory*, vol. 52, no. 2, pp. 489–509, 2006.

[10] E. J. Candès, J. K. Romberg, and T. Tao, "Stable signal recovery from incomplete and inaccurate measurements," *Communications on pure and applied mathematics*, vol. 59, no. 8, pp. 1207–1223, 2006.

[11] E. J. Candès and T. Tao, "Near-optimal signal recovery from random projections: Universal encoding strategies?," *IEEE Transactions on Information Theory*, vol. 52, no. 12, pp. 5406–5425, 2006.

[12] M. Lustig, D. Donoho, and J. M. Pauly, "Sparse MRI: The application of compressed sensing for rapid MR imaging," *Magnetic Resonance in Medicine*, vol. 58, no. 6, pp. 1182–1195, 2007.

[13] J. D. Jackson, *Classical electrodynamics*. New York, NY: John Wiley & Sons, Inc, 3rd ed., 1999.

[14] F. Jensen and A. Frandsen, "On the number of modes in spherical wave expansions," in *26th Annual Meeting and Symposium of the Antenna Measurement Techniques Association*, (Stone Mountain Park, GA, USA), pp. 489–494, 2004.

[15] D. L. Donoho, "Compressed sensing," *IEEE Transactions on Information Theory*, vol. 52, no. 4, pp. 1289–1306, 2006.

[16] *IEEE Standard Definitions of Terms for Antennas*, 1993. IEEE Std 145-1993.

[17] C. A. Balanis, *Antenna Theory: Analysis and Design*. New York, NY: John Wiley & Sons, Inc, 2nd ed., 1997.

[18] E. J. Candès, "Compressive sampling," in *Proceedings of the International Congress of Mathematicians*, vol. 3, (Madrid, Spain), pp. 1433–1452, 2006.

[19] R. F. Harrington, "On the gain and beamwidth of directional antennas," *IRE Transactions on Antennas and Propagation*, vol. 6, no. 3, pp. 219–225, 1958.

[20] R. C. Wittmann, C. F. Stubenrauch, and M. H. Francis, "Using truncated data sets in spherical-scanning antenna measurements," *International Journal of Antennas and Propagation*, vol. 2012, 2012.

[21] E. Martini, S. Maci, and L. J. Foged, "Spherical near field measurements with truncated scan area," in *Proceedings of the 5th European Conference on Antennas and Propagation*, (Rome, Italy), pp. 3256–3258, 2011.

[22] L. Foged, L. Scialacqua, F. Saccardi, F. Mioc, J. A. Quijano, E. Martini, S. Maci, M. Sabbadini, and G. Vecchi, "Comparative investigation of methods to reduce truncation errors in partial spherical near-field antenna measurements," in *6th European Conference*

on Antennas and Propagation, (Prague, Czech Republic), pp. 2533–2537, 2012.

[23] E. Candès and J. Romberg, "l_1-magic: Recovery of sparse signals via convex programming." `http://users.ece.gatech.edu/justin/l1magic/#papers`, 2005. [Online; accessed 17-March-2016].

[24] D. L. Donoho, A. Maleki, and A. Montanari, "Message-passing algorithms for compressed sensing," *Proceedings of the National Academy of Sciences*, vol. 106, no. 45, pp. 18914–18919, 2009.

[25] S.-J. Kim, K. Koh, M. Lustig, S. Boyd, and D. Gorinevsky, "An interior-point method for large-scale l_1-regularized least squares," *IEEE Journal of Selected Topics in Signal Processing*, vol. 1, no. 4, pp. 606–617, 2007.

[26] K. Koh, S.-J. Kim, and S. Boyd, "`l1_ls`: Simple Matlab solver for l_1-regularized least squares problems." `https://stanford.edu/~boyd/l1_ls/`, 2008. [Online; accessed 17-March-2016].

[27] S. Boyd and L. Vandenberghe, *Convex optimization*. New York, NY, USA: Cambridge University Press, 2004.

DECLARATION

Hiermit erkläre ich, dass die vorliegende Arbeit gemäß dem Code of Conduct – Regeln zur Sicherung guter wissenschaftlicher Praxis (in der aktuellen Fassung des jeweiligen Mitteilungsblattes der TU Wien), insbesondere ohne unzulässige Hilfe Dritter und ohne Benutzung anderer als der angegebenen Hilfsmittel, angefertigt wurde. Die aus anderen Quellen direkt oder indirekt übernommenen Daten und Konzepte sind unter Angabe der Quelle gekennzeichnet.

Die Arbeit wurde bisher weder im In- noch im Ausland in gleicher oder in ähnlicher Form in anderen Prüfungsverfahren vorgelegt.

Vienna, June 2016

David Löschenbrand